



## Article

# Deciphering the pressure–temperature path in low-grade metamorphic rocks by combining crystal chemistry, thermobarometry and thermodynamic modelling: an example in the Marguareis Massif, Western Ligurian Alps, Italy

Edoardo Sanità<sup>1</sup> , Maria Di Rosa<sup>2</sup> , Jean Marc Lardeaux<sup>2,3</sup> , Michele Marroni<sup>1,4</sup> , Marco Tamponi<sup>1</sup> ,  
Marco Lezzerini<sup>1</sup>  and Luca Pandolfi<sup>1</sup> 

<sup>1</sup>Dipartimento di Scienze della Terra, Università di Pisa, Pisa, Italia; <sup>2</sup>UMR Géosciences Azur, Université de la Côte d'Azur, Nice-Sophia Antipolis, France; <sup>3</sup>Centre for Lithospheric Research, Czech Geological Survey, Prague 1, 118 21, Czech Republic; and <sup>4</sup>Consiglio Nazionale della Ricerca, Istituto di Geoscienze e Georisorse, IGG-CNR, Pisa, Italia

### Abstract

Unveiling the pressure–temperature path of low-grade metamorphic rocks is challenging because of the occurrence of detrital minerals and high-variance mineral assemblages (i.e. chlorite–white mica–quartz). This paper is an attempt to reconstruct the pressure–temperature history on metapelites from a low-grade metamorphic unit, i.e. the Cabanaira Unit, located in the Marguareis Massif (Western Ligurian Alps, Italy). In order to obtain the most robust result possible, multi-equilibrium thermobarometry, forward modelling and crystallochemical index measurements are used together to reconstruct a pressure–temperature path, with consideration of the strengths and weaknesses of these methods.

This multidisciplinary approach allowed us to reconstruct the metamorphic evolution of the unit of interest, characterised by a pressure peak reached under low-temperature conditions (0.85–0.68 GPa and 250–285°C) followed by decompressional warming (low pressure–high temperature, 0.4–0.6 GPa and 300–335°C).

This pressure–temperature path is consistent with the tectonic evolution of the investigated area proposed by previous studies, where a geological scenario in which the Cabanaira Unit experienced subduction-related processes was postulated, even if the reasons for warming remain unclear.

Multi-equilibrium thermobarometry is considered to be the most suitable method to unravel the metamorphic history of low-grade rocks, whereas forward thermodynamic modelling and the calculation of crystallochemical indexes seem to resolve only some segments of the pressure–temperature path.

**Keywords:** low-grade rocks; thermobarometry; crystallochemical indexes; thermodynamic modelling; Marguareis Massif; Southwestern Alps

(Received 15 May 2024; accepted 8 October 2024; Accepted Manuscript published online: 12 November 2024)

### Introduction

In recent decades, the quantification of intensive parameters of metamorphism has undergone remarkable evolution with the production of internally consistent thermodynamic databases (Berman, 1988; Holland and Powell, 1998, 2011) and the improvement of our understanding of mixing properties and

activity–composition relationships for mineral solid solutions and melts (Green *et al.*, 2016; White *et al.*, 2014). The development of software using these various databases has had a significant impact on modelling the thermodynamic evolution of metamorphic rocks (Powell *et al.*, 1998; Connolly, 2005; De Capitani and Petrakakis, 2010; Duesterhoeft and Lanari, 2020; Xiang and Connolly, 2022). These approaches allow the stability fields, mode and composition of minerals to be estimated for a given rock composition in the pressure–temperature ( $P$ – $T$ ) space (Thinkam and Ghent, 2005; Powell *et al.*, 2005; Spear *et al.*, 2016; Lanari and Duesterhoeft, 2019; Lanari *et al.*, 2019). This, together with decisive progresses in ‘*in situ*’ geochronology has allowed better understanding of the tectono-metamorphic evolution of high-grade units. (Štípská *et al.*, 2016; Plunder *et al.*, 2012; Airaghi *et al.*, 2017; Luoni *et al.*,

**Corresponding author:** Michele Marroni; Email: [michele.marroni@unipi.it](mailto:michele.marroni@unipi.it)

**Associate Editor:** Thomas Mueller

**Cite this article:** Sanità E, Di Rosa M, Lardeaux JM, Marroni M, Tamponi M, Lezzerini M and Pandolfi L (2025). Deciphering the pressure–temperature path in low-grade metamorphic rocks by combining crystal chemistry, thermobarometry and thermodynamic modelling: an example in the Marguareis Massif, Western Ligurian Alps, Italy. *Mineralogical Magazine*, 1–22. <https://doi.org/10.1180/mgm.2024.80>

2019; Lotout *et al.*, 2020; Ghignone *et al.*, 2021; Bonnet *et al.*, 2022; Collett *et al.*, 2022). In contrast, poor thermomechanical constraints on the tectonic evolution of low- and very low-grade metamorphic units involved in external collision zones were implemented (Muirhead *et al.*, 2020 and quoted references; Willner, 2021). Currently, electron probe microanalysis (EPMA) provides high-quality reliable and reproducible compositional analysis, even on fine-grained minerals that are generally present in low-grade metamorphic rocks (see Lanari *et al.*, 2012; Airaghi *et al.*, 2017; Di Rosa *et al.*, 2019; Sanità *et al.*, 2022b, 2022c; Barbero *et al.*, 2023). This has led metamorphic petrologists to investigate a larger dataset of metasedimentary rocks, opening new scenarios for understanding low-grade metamorphism based on robust  $P$ – $T$  estimations (i.e. Massonne and Schreyer, 1987; Vidal *et al.*, 1999; Vidal and Parra, 2000; Parra *et al.*, 2002; Agard *et al.*, 2001; Vidal *et al.*, 2005; Dubacq *et al.*, 2010; Pourteau *et al.*, 2014; Lanari *et al.*, 2014a; Bourdelle and Cathelineau, 2015). Among metasedimentary rocks, metapelites are widely represented lithotypes in mountain belts. The difficulty in studying this kind of metamorphic rock is related to the occurrence of detrital minerals, which remain as relict phases without reacting during metamorphism, thus making the reactive bulk composition difficult to investigate (Tracy, 1982; Marmo *et al.*, 2002; Tinkham and Ghent, 2005; Lanari and Engi, 2017). Therefore, a combination of careful microstructural investigations and various thermodynamic methods are required to constrain the  $P$ – $T$  paths recorded by these rocks.

In this study, we present an attempt to reconstruct a  $P$ – $T$  path by combining crystallochemical indexes and thermodynamic modelling including multi-equilibrium thermobarometry and phase equilibria relationships (i.e. pseudosections). This approach is tested in metapelites sampled in a low-grade unit, i.e. the Cabanaira Unit, located in the High Valle Roja in the southwestern sector of the Marguareis Massif along the Italian–French border (Western Ligurian Alps, Fig. 1). The reconstructed  $P$ – $T$  path is then discussed to evaluate its consistency with respect to the available regional tectonic framework of the investigated area.

## Geology of the sampling area

The samples investigated were collected in the Cabanaira area within the Marguareis Massif. This massif is located along the Western Ligurian Alps which are part of the southwestern prolongation of the Alpine collisional belt (Fig. 1a,b). The latter is characterised by a long-lived convergence history between the Europe and Adria Plates (Handy *et al.*, 2010; Schmid *et al.*, 2017; Manatschal *et al.*, 2022). This history commenced in the Late Cretaceous with a subduction system leading to progressive consumption of the Ligure–Piemontese Ocean (ocean subduction stage), which was interposed between the two plates (Stampfli *et al.*, 2001; Beltrando *et al.*, 2010; Lardeaux, 2014; Lagabrielle *et al.*, 2015; Marotta *et al.*, 2018; Roda *et al.*, 2019), and part of the Adria Plate (Polino *et al.*, 1990; Lardeaux and Spalla, 1991; Stöckhert and Gerya, 2005). Subsequently, after the closure of the Ligure–Piemontese Ocean, the European continental crust started to be involved in a subduction system (continental subduction stage, Rosenbaum *et al.*, 2002; Handy *et al.*, 2010; Schmid *et al.*, 2017) in the Eocene until continental collision occurred during the early Oligocene (collision stage, Ford *et al.*, 2006; Simon-Labric *et al.*, 2009). Finally, tectonic denudation started during the Miocene (Tricart *et al.*, 2001).

According to the classic tectonic framework proposed for the southwestern Alps (Vanossi *et al.*, 1984; Seno *et al.*, 2005; Seno *et al.*, 2003; Bonini *et al.*, 2010; Mueller *et al.*, 2020), their westernmost part (outer sectors) is characterised by a SW-verging fold-and-thrust belt consisting of the Dauphinois/Provençal Units, which, together with the External Crystalline Massifs, represent the former European continental margin, poorly involved in the Alpine collisional stage. These units are separated by the southern prolongation of the Penninic Front, whose activity is constrained at 33 Ma in this sector of the belt (Maino *et al.*, 2015), from the Briançonnais Units (Fig. 1a, see Sanità *et al.*, 2021, 2023). The latter, together with the Internal Crystalline Massifs (blue domains of Fig. 1a), are classically regarded as the thinned portion of the European continental margin that was deeply involved in continental subduction, which is documented for the whole Western Alps (Michard *et al.*, 2004; Bousquet *et al.*, 2008; Lanari *et al.*, 2012; Strzeczynski *et al.*, 2011; Groppo *et al.*, 2019; Manzotti *et al.*, 2022; Sanità *et al.*, 2022b). They are thrust in turn by oceanic-derived units representative of the Ligure–Piemontese Ocean (i.e. the Moglio–Testico and the Borghetto d'Arroschia Units, Vanossi *et al.*, 1984; Di Giulio, 1988; Di Giulio, 1992; Mueller *et al.*, 2020; Sanità *et al.*, 2022c; and the Voltri Group, Chiesa *et al.*, 1975; Capponi and Crispini, 2002; Capponi *et al.*, 2009). The San Remo–Monte Saccarello Unit, whose paleogeographic origin is a matter of debate (Sagri, 1984; Mueller *et al.*, 2018; Sanità *et al.*, 2021a; Sanità, 2023), forms the uppermost portion of the tectonic pile (Fig. 1a–c, see also Maino and Seno, 2016 and Mueller *et al.*, 2020). Moving towards the Ligurian Sea, the San Remo–Monte Saccarello Unit tectonically overlays the Dauphinois/Provençal Units (Fig. 1a–c see also Perotti *et al.*, 2012; Decarlis *et al.*, 2013; Mueller *et al.*, 2020).

In the sampling area, the Cabanaira Unit (cf. Roja Unit of Piana *et al.*, 2014 and Rocca-Borbone Unit of Maino and Seno, 2016) is separated, to the east, by the Penninic Front from a SW-verging stack of units (according to Sanità *et al.*, 2021a, 2021b; Figs 1b,d). The latter, from the upper to the lower structural levels, consists of: (1) the topmost Marguareis Unit (Briançonnais Domain), regarded as a fragment of the European continental margin involved in the subduction zone (Carminati, 2001; Decarlis *et al.*, 2013; Sanità *et al.*, 2021a; 2021b) that experienced high pressure–low temperature ( $HP$ – $LT$ ) metamorphism (1.0–0.9 GPa and 280–330°C, Sanità *et al.*, 2022b); (2) the Helminthoid Flysch Unit (cf. San Remo–Monte Saccarello Unit of Sagri, 1984), which is here considered as being derived from the External Ligurian Domain (according to Sanità *et al.*, 2021a, 2022a; Sanità, 2023) and has a diagenetic/anchizone-type metamorphic imprint ( $T$  never exceeding 220°C, Piana *et al.*, 2014; Maino *et al.*, 2020 and  $P$  in the range of 0.5–0.2 GPa, Sanità, 2023). To the southeast, the oceanic-derived Moglio–Testico Unit crops out (Fig. 1d), which is tectonically located between the Marguareis Unit and the Helminthoid Flysch and has a  $HP$  metamorphic imprint achieved during the oceanic subduction stage (1.2–1.0 GPa and 260–330°C, Sanità *et al.*, 2022c).

According to Sanità *et al.* (2021a), the Cabanaira Unit (Fig. 2a) consists of a Jurassic platform meta-carbonate (Forte Pepin Limestone, FPL) unconformably underlying the middle Eocene (Gidon, 1972) *Nummulites*-rich meta-limestones (Nummulitic Limestone, NUM) and foredeep meta-turbidites (Cima Aurusi Formation, CAF). The finite strain pattern of the Cabanaira Unit, which records the superposition of folding and thrusting events (Sanità *et al.*, 2021a, 2021b), is thought to be the result of its involvement in alpine convergent-related processes. The oldest deformation event (here D1 phase, cf. D1<sub>CU</sub> 'pre-stacking

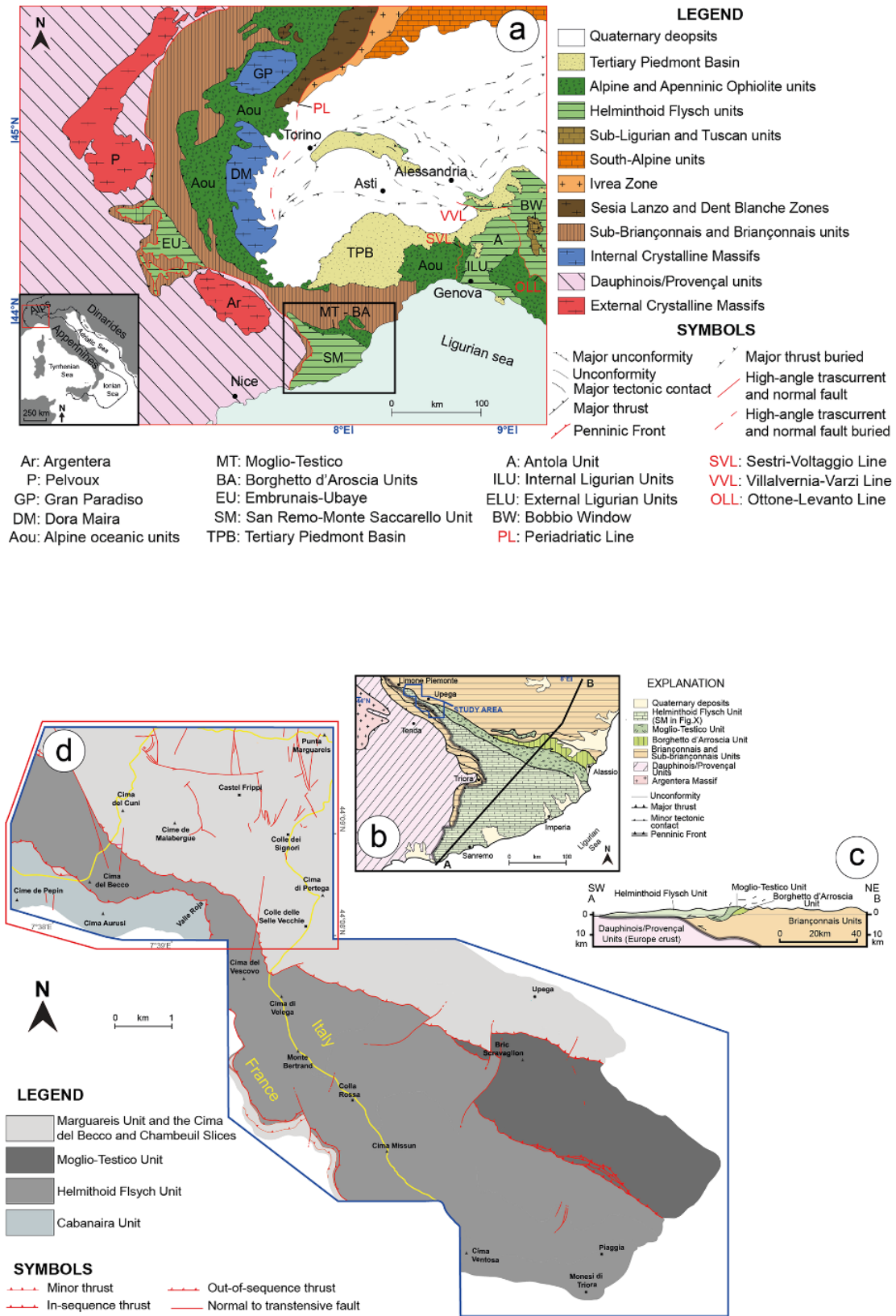


**Figure 1.** (a) Geological scheme of the Western Alps-Northern Apennines (modified and re-drawn from Molli *et al.*, 2010 and Sanità *et al.*, 2021a). (b) Close-up of the Western Ligurian Alps (black box of a) with the related geological cross-section (c) modified by Bonini *et al.* (2010). (d) Simplified geological sketch (blue box of b) of the boundary between Maritime and Ligurian Alps.

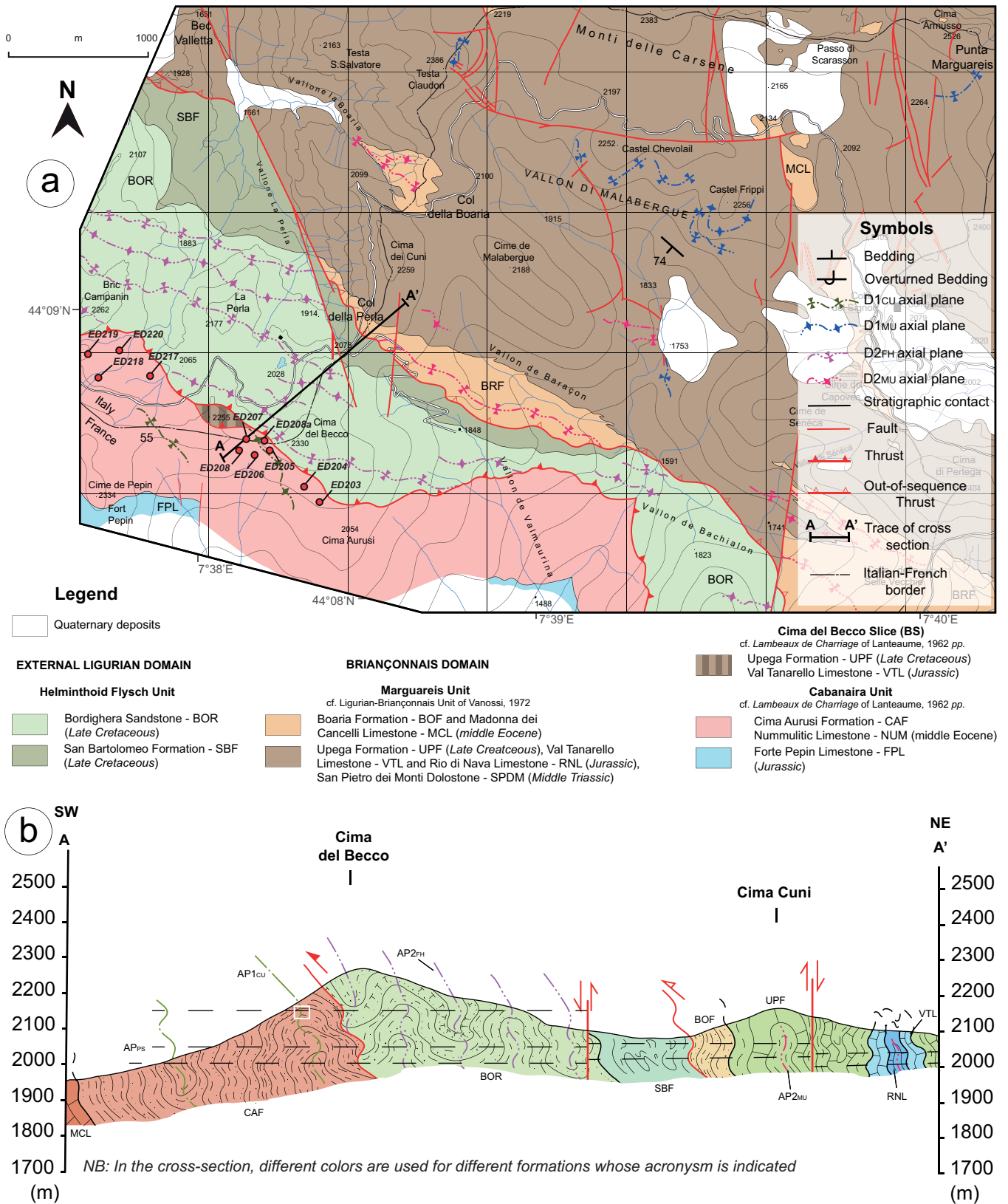


**Figure 2.** (a) Geological map (modified from Sanità et al., 2021a and 2021b) of the Marguareis Massif (red box of Fig. 1d) with the related geological cross-section (b). In the map the locations of samples are reported (red dots).

structures' of Sanità et al., 2021a) produced a SW-verging folding system that was confined within the unit and developed from

micro- to map-scale (Figs 2b, 3a). The associated axial planes were cut by the subsequent deformation event ('syn-stacking event' of

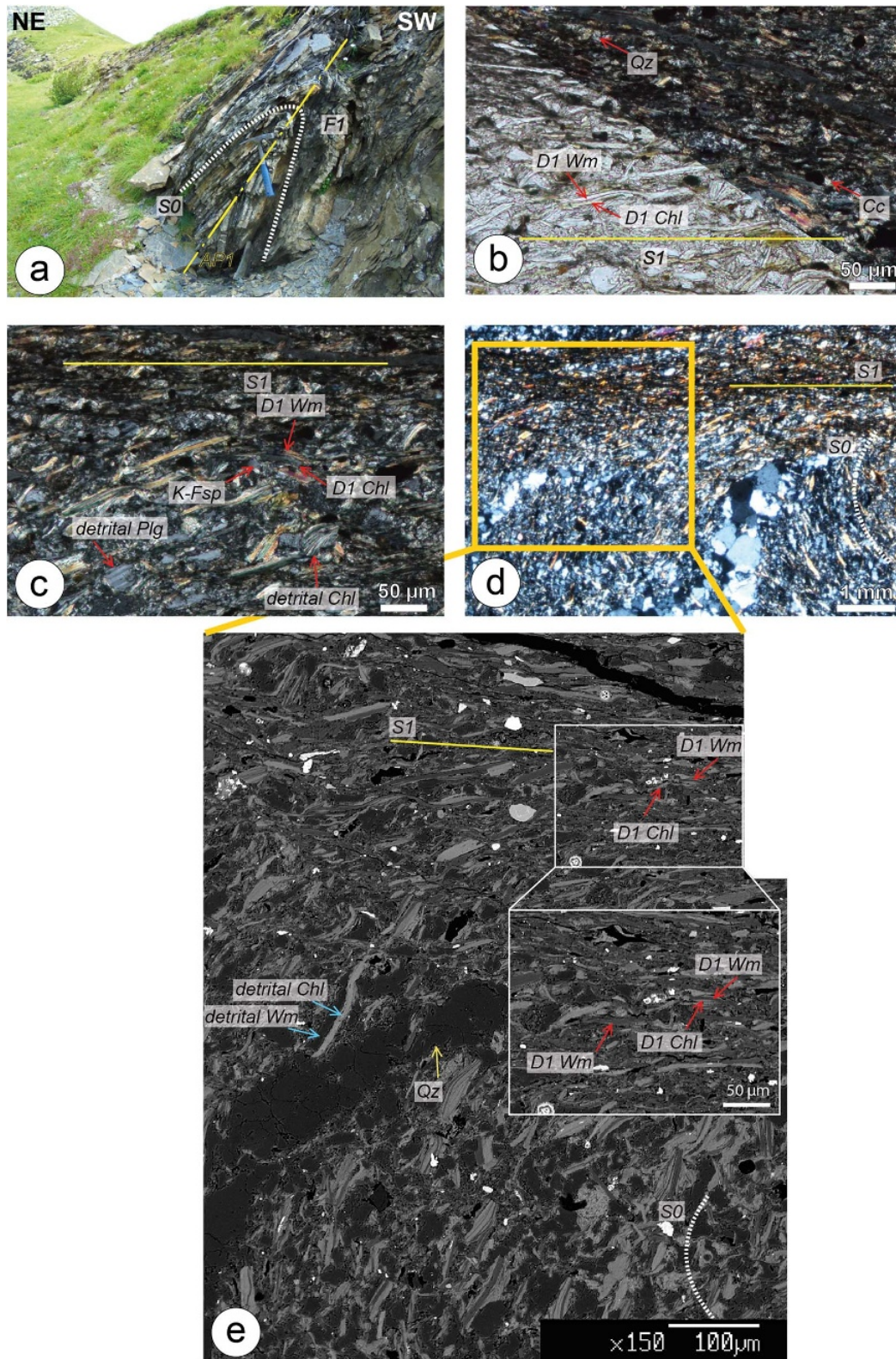


**Figure 3.** Macro- to micro-scale D1 phase-related structural features. (a) F1 fold system in the Cabanaira Unit (white box of Fig. 2b). (b, c) S1 (yellow line) slaty cleavage (bottom left of b: plane polarized light, top right of b and c: crossed polarized light) marked by syn metamorphic Wm and Chl and Qz in textural equilibrium. Detrital grains of plagioclase and chlorite (c) can be observed. (d) Microphotograph of F1 hinge-zone where clear cross-cutting relationships between S1 (yellow line) and bedding (S0, white dashed line) are shown. (e) BSE image of the micro-area investigated to perform the *P-T* estimates (orange box of d). The white box represents the area where the local bulk composition was extracted to perform forward and inverse thermodynamic modelling. Along the S0 (white dashed line), detrital Wm and Chl (blue arrows) are indicated. Along the S1 (yellow line) neo-formed Wm and Chl crystals (red arrows in the white boxes) are present.

Sanità *et al.*, 2021a), which was responsible for the thrusting of the Helminthoid Flysch Unit onto the already deformed Cabanaira Unit (see geological cross-section of Fig. 2b). The last deformation events are represented by a fold system (here called the D2 phase, cf. 'post-stacking folds' of Sanità *et al.*, 2021a) with roughly flat-lying axial planes and high-angle faults. D1-related folding produced isoclinal to tight F1 folds that are associated with S1 tectonic foliation (Figs 2b, 3a). At the outcrop scale, this foliation is a continuous surface that is well developed in fine-grained rocks (i.e. metapelites), whereas in the more competent layers (e.g. limestones), it appears as a spaced cleavage or, as in other cases, it is scarcely preserved.

## Materials and methods

### Materials

To perform this study, we collected samples where the S1 foliation is well preserved, i.e. the metapelites from the topmost deposits (Cima Aurusi Formation) of the Cabanaira Unit. In these specimens, the S1 foliation is a slaty cleavage developed by pressure solution processes (i.e. pressure solution creep) that are diagnostic for fluid-assisted deformation under low-temperature conditions (Rutter, 1983; Gratier *et al.*, 2013 with references therein). Parallel to this dissolution schistosity plane white mica (Wm), chlorite (Chl) and quartz (Qz) (mineral abbreviations after Warr, 2021 with the exception of white mica) with marked shape-preferred orientation are typically well developed. Moreover, there are ultra-local micro-domains where grains of Wm + Chl + Qz ± calcite (Cc) and potassic feldspar (K-Fsp) can be observed (Fig. 3b–d) showing clear textural equilibrium relationships suggesting that metamorphic crystallization of new grains occurred along the S1 foliation. Along the S1 foliation, syn-metamorphic elongated Wm grains have lengths not exceeding 15–25 µm (Fig. 3b–e), whereas Chl grains are stubby, sometimes with recrystallized tails, reaching up to 30 µm in size (Fig. 3b–e). Both have undulose extinction and well defined edges with apparently no evidence of compositional zoning (Fig. 3b,c). Large and altered Wm and Chl crystals (both greater than 60 µm in length) with frayed edges and slight compositional zoning are also present (Fig. 3e) in which the micro-textures suggest a detrital origin. The latter are mostly set along the primary bedding (S0 in Fig. 3d,e) and show clear cross-cutting relationships with the syn-metamorphic mineral growth along the S1 foliation (Fig. 3d,e). Plagioclase (albite?, Fig. 3c) are also present and are characterised by stubby grains with frayed edges wrapped by very fine-grained crystals of Wm and Chl and indicating a detrital nature. In accord with the above microstructural observations the main deformation mechanisms include re-crystallization, pressure solution and passive rotation of detrital phyllosilicates (according to Groshong, 1988; Hirt and Tullis, 1992; Passchier and Trouw, 2005).

### Methodological approach

Microstructures and micro-textures were the main criteria used to select the microdomains characterised by dynamic recrystallization of Wm and Chl with which the *P* and *T* conditions were estimated (white box of Fig. 3e, see also the next section). Figure 3e shows the micro-area (orange box in Fig. 3d) chosen to perform the *P–T* investigation. The microdomain of Fig. 3d (detail in X-ray maps in Fig. 4a,b) was chosen in order to include neoformed grains of Chl and Wm and Qz, which grew along the

S1 foliation, avoiding detrital grains (Fig. 3d,e). In the selected micro-area, syn-metamorphic Chl and Wm (white box of Fig. 3e) are slightly zoned with rims slightly brighter than cores. Wm and Chl grains occur either as well-defined grains or very fine-grained crystals.

As the detrital minerals cannot be excluded as relict phases in the micro-domain of interest, and because of the high-variance Chl–Wm–Qz mineral assemblage, different analytical techniques, including inverse multi-equilibrium thermobarometry and forward modelling (i.e. pseudosections), a Wm 'crystallinity' index (WmIC) and  $b_0$  cell parameters were used. Eleven samples of metapelites (Fig. 2a, the geographic coordinates of each sample are available in table T1 in Supplementary materials S1) were selected for measurements. Thermobarometric estimates and forward modelling were performed using X-ray compositional maps on one sample of metapelite collected in the F1 hinge zone (sample ED208a), whereas the WmIC values were measured on 10 samples of carbonate-free metapelite powders (ED203–208 and ED2017–220). The WmIC (Kubler, 1967a, 1967b) and the  $b_0$  cell parameter (Guidotti and Sassi, 1986; Guidotti *et al.*, 1989; Franceschelli *et al.*, 1989) are primarily known as qualitative methods and are thought to be functions of *T* and *P*, respectively. In this work, the *T* and *P* ranges obtained from the WmIC and  $b_0$  cell parameters were compared with the results of the other independent methods applied (Guidotti and Sassi, 1998; Kubler and Goy-Eggenberger, 2001; Abad and Nieto, 2007; Warr and Ferreiro Mählmann, 2015).

### X-ray map processing and local bulk composition

The X-ray map was obtained using a JEOL 8800 electron microprobe at the Dipartimento di Scienze della Terra "A. Desio" (Milano, Italy), equipped with five wavelength-dispersive spectrometers and calibrated with the following standards: wollastonite (Ca, Si); orthoclase (K); albite (Al); periclase (Mg); rhodonite (Mn); TiO<sub>2</sub> (Ti); Al<sub>2</sub>O<sub>3</sub> (Al); Fe<sub>2</sub>O<sub>3</sub> (Fe); and Cr<sub>2</sub>O<sub>3</sub> (Cr) (for the acquisition settings see supplementary material S2, for the position of each spot analysis within the investigated micro-area see tables T2 and T3 and fig. F1). The X-ray intensities were processed with *XMapTools* 3.2 software (Lanari *et al.*, 2014b) to produce an oxide composition (wt.%) quantitative map using the spot analyses (see supplementary tables T2 and T3 in S2 for criteria used to evaluate the quality of standard analysis) as an internal standard following the procedure described by De Andrade *et al.* (2006). The Local Bulk Composition (LBC) of the selected micro-area (white box of Fig. 3e) was obtained using the *density-corrected oxide map* function implemented in the *XMapTools* program (see the supplementary material S2 for details about the adopted procedure).

### Forward modelling

Forward phase equilibria modelling was performed in order to evaluate the equilibrium of the metamorphic minerals that have grown along the S1 foliation using the LBC extrapolated from the wt.% map (Lanari and Engi, 2017, see table T4 in supplementary material S3). The Gibbs free energy minimization algorithm of Theriak-Domino (de Capitani and Petrakakis, 2010), was used to compute isochemical phase diagrams and mineral compositional isopleths of Wm and Chl with or without the ferric iron content. The internally consistent thermodynamic database *JUN92.bs* (Berman, 1988; Pourteau *et al.*, 2014) implemented with the solution models of Parra *et al.* (2002) with the revised Margules parameters for Wm (Dubacq *et al.*, 2010), Chl (Vidal *et al.*, 2005),

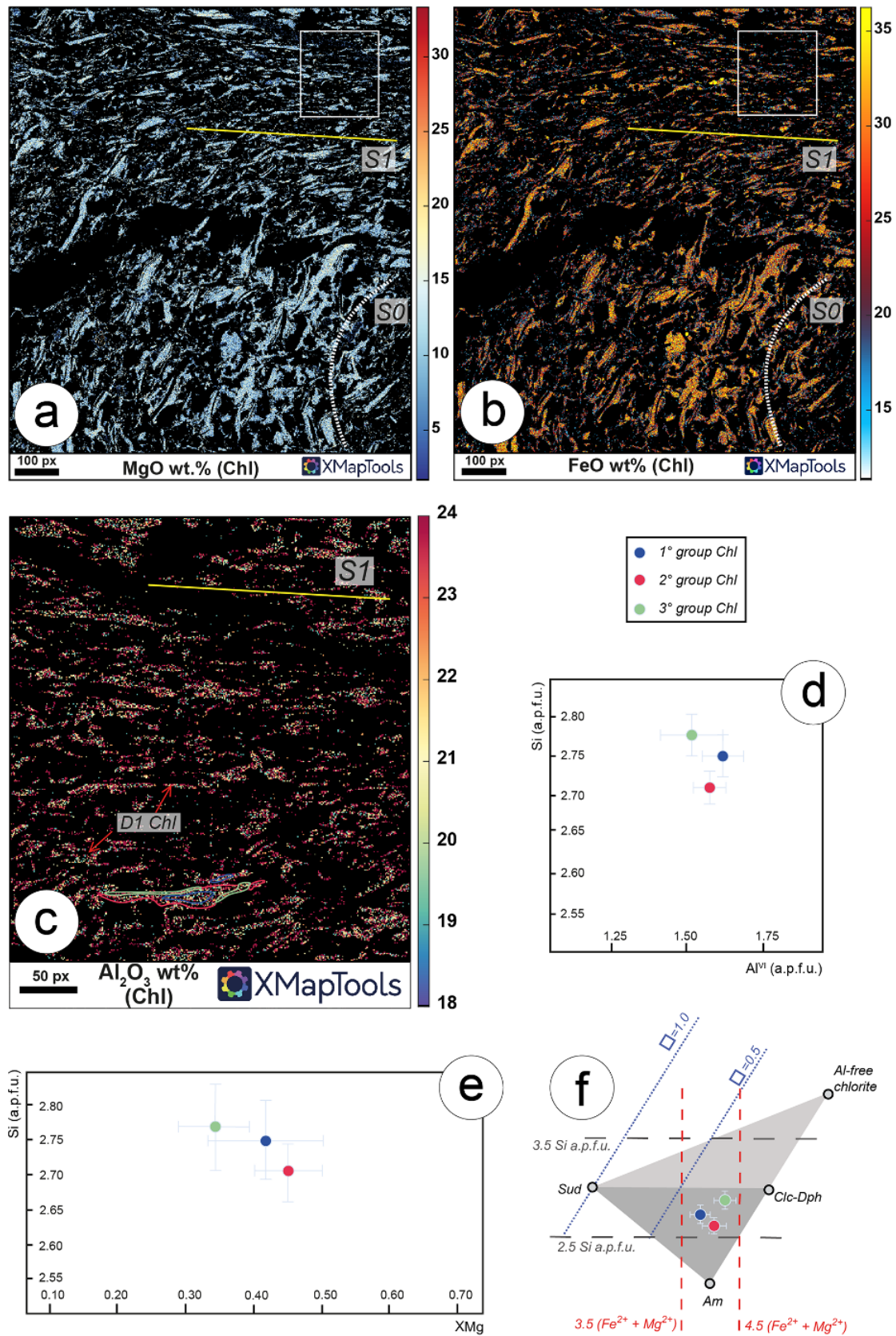


**Figure 4.** Composition of chlorites in ED208a sample. MgO wt.% (a) and FeO wt.% variation in the microdomain signalled in Fig. 3e. Differences exist between detrital (white dotted line) and syn-metamorphic (yellow line) Chl grains. (c) Enlarged area of the white box of (a) and (b) of the syn-metamorphic Chl (red arrows) grew along the S1 foliation (yellow line). The Al<sub>2</sub>O<sub>3</sub> wt.% variation sheds light on the complex mineral chemistry of the neo-formed grains (blue, red and green areas) corresponding to first, second and third groups (see the text). (d) Al<sup>VI</sup>/Si and (e) XMg/Si plots referred to the average compositions of the three groups of Chl detected along the S1 foliation are reported with their error bars. (f) Octahedral Fe<sup>2+</sup> + Mg<sup>2+</sup> (apfu, red dashed lines) content vs. Si (grey dashed lines) diagram (according to Bourdelle and Cathelineau, 2015). The blue dotted lines show the octahedral vacancy (blue empty squares) values. The four Chl end-members are also reported.

**Table 1.** Average compositions (wt.%) related to the three groups of Chl. Standard deviation is indicated

	1° group Chl*		2° group Chl*		3° group Chl*	
SiO <sub>2</sub>	25.85	±2.21	25.85	±2.79	25.85	±1.24
TiO <sub>2</sub>	< 0.01		0.12	±0.10	< 0.01	
Al <sub>2</sub> O <sub>3</sub>	22.99	±0.56	23.27	±0.40	2.87	±2.38
FeO	27.19	±2.27	26.05	±1.60	31.72	±3.20
MnO	0.04	±0.04	0.06	±0.03	0.08	±0.00
MgO	10.89	±2.50	12.08	±1.77	9.17	±1.18
CaO	0.17	±0.07	0.17	±0.05	0.09	±0.04
Na <sub>2</sub> O	< 0.01		< 0.01		< 0.01	
K <sub>2</sub> O	0.34	±0.34	0.21	±0.24	0.17	±0.08
Total	88.66	±1.18	89.21	±0.83	88.94	±0.39
Si	2.75	±0.06	2.72	±0.04	2.77	±0.07
Al <sup>IV</sup>	1.25	±0.06	1.28	±0.04	1.23	±0.07
Al <sup>VI</sup>	1.63	±0.06	1.60	±0.04	1.52	±0.16
Ti	-		0.00	±0.01	0.00	
Fe <sub>tot</sub>	2.42	±0.26	2.29	±0.18	2.84	±0.36
Mn	0.00	±0.00	0.01	±0.00	0.01	±0.00
Mg	1.73	±0.36	1.89	±0.25	1.46	±0.15
Ca	0.02	±0.00	0.02	±0.01	0.01	±0.00
Na	n.d.		n.d.		n.d.	
K	0.05	±0.05	0.03	±0.02	0.02	±0.00
M-site	5.79	±0.04	5.79	±0.03	5.83	±0.05
sum cations	9.85	±0.85	9.88	±0.59	9.87	±0.81
vacancy	0.19	±0.06	0.16	±0.04	0.15	±0.04
XMg	0.42	±0.08	0.45	±0.05	0.34	±0.05
Clin + Daph	0.53	±0.03	0.50	±0.02	0.59	±0.12
Am	0.28	±0.09	0.34	±0.06	0.26	±0.07
Sud	0.19	±0.06	0.16	±0.04	0.15	±0.04

\*average and standard deviation were obtained from 50 analysis for group from *XMapTools*. n.d. - not detected

carpholite (solution models of Vidal *et al.*, 1992; Dubacq, 2008) and chloritoid (solution models of Vidal *et al.*, 2001) were used to perform all of the computations (see the supplementary material S3 for details about the solution models included in the database) with an excess of H<sub>2</sub>O-rich fluid (aH<sub>2</sub>O = 0.8).

### Thermobarometry

The multi-equilibrium modelling approach for partially re-equilibrated minerals (this study) allows us to detect different segments of the *P-T* path (i.e. peak *P*, peak *T*; in accord with Lanari and Duesteroth, 2019). Therefore, to estimate the *P* and *T* conditions recorded by the Cabanaira Unit, chemical analyses of Chl and Wm grains grown along the S1 foliation were processed with three different methods using *ChlMicaEqui* software (Lanari, 2012), which operates assuming the presence of water (H<sub>2</sub>O) and Qz within the assemblage. In the calibrated compositional map (Fig. 4a), we investigated the micro-area where the relationships between the identified S1 foliation and the primary bedding (white box in Fig. 3e) were unambiguously clear. In this microdomain, we considered all chemical heterogeneity of Chl and Wm using the *XMapTools* software (Lanari *et al.*, 2014b). This operation allowed us to investigate analytical results for each neo-formed mineral phase (Chl and Wm) avoiding the detrital crystals (Tables 1 and 2). The methods used to retrieve the *P-T* equilibrium conditions are the Chl-Qz-H<sub>2</sub>O, the Phg-Qz-H<sub>2</sub>O and the Chl-Phg-Qz-H<sub>2</sub>O methods.

**Table 2.** Average compositions related to the three groups of Wm. Standard deviation is indicated

	1° group Wm*		2° group Wm*		3° group Wm*	
SiO <sub>2</sub>	48.61	±2.03	45.68	±3.51	46.56	±1.24
TiO <sub>2</sub>	0.14	±0.07	0.00		0.27	±0.18
Al <sub>2</sub> O <sub>3</sub>	28.13	±3.16	31.05	±3.16	32.33	±2.33
FeO	5.72	±1.17	4.04	±2.67	4.04	±1.43
MnO	0.02	±0.00	0.01	±0.01	< 0.01	
MgO	2.71	±0.58	2.38	±1.47	2.04	±0.72
CaO	0.02	±0.02	0.27	±0.38	0.02	±0.02
Na <sub>2</sub> O	< 0.01		< 0.01		< 0.01	
K <sub>2</sub> O	9.03	±3.13	10.61	±1.03	11.51	±0.01
Total	94.25	±2.63	94.03	±5.48	96.76	±0.03
Si	3.31	±0.02	3.14	±0.08	3.11	±0.10
Al <sup>IV</sup>	0.69	±0.02	0.86	±0.08	0.89	±0.10
Al <sup>VI</sup>	1.56	±0.10	1.64	±0.09	1.66	±0.07
Ti	0.01	n.d.	n.d.	n.d.	0.01	n.d.
Fe <sub>tot</sub>	0.32	±0.07	0.24	±0.18	0.23	±0.08
Mn	n.d.	n.d.	n.d.	n.d.	n.d.	
Mg	0.28	±0.08	0.24	±0.14	0.20	±0.07
Ca	n.d.	n.d.	0.02	±0.01	n.d.	n.d.
Na	n.d.		n.d.		n.d.	
K	0.79	±0.30	0.93	±0.03	0.98	±0.01
A site	0.79	±0.30	0.95	±0.05	0.98	±0.01
M-site	2.17	±0.08	2.13	±0.11	2.11	±0.04
sum cations	2.96	±0.33	3.07	±0.16	3.09	±0.05
vacancy	0.20	±0.15	0.05	±0.05	0.02	±0.01
XMg	0.46	±0.10	0.52	±0.22	0.48	±0.18
Ms	0.52	±0.09	0.73	±0.06	0.77	±0.08
Cel	0.20	±0.15	0.16	±0.13	0.11	±0.13
Prl	0.20	±0.12	0.08	±0.01	0.02	±0.01
Trioct.	0.17	±0.08	0.13	±0.11	0.11	±0.04

\*average and standard deviation were obtained from 50 analysis for group from *XMapTools*. n.d. - not detected

The Chl-Qz-H<sub>2</sub>O method (Vidal *et al.*, 2006) has been used to calculate the temperature range for chlorite formation (see supplementary material S4 for more details about this geothermometer), with an equilibrium tolerance of 30°C for estimating the percentage of Fe<sup>3+</sup> for each Chl analysis with fixed pressure value (see F2 in supplementary S4) and specific water activity (0.8 for the presence of Cc, according to Frassi *et al.*, 2022).

The Phg-Qz-H<sub>2</sub>O method (Dubacq *et al.*, 2010) relies on the de-hydration of Wm to refine the thermodynamic status of water, and is based on temperature-sensitive reactions (see supplementary material S4 for more details about this method). However, *P* also affects the reaction and, therefore, for a fixed *T*, the percentage of Fe<sup>3+</sup> content and *P* can be estimated simultaneously (see Lanari, 2012; Scheffer *et al.*, 2016; Lanari *et al.*, 2019; Di Rosa *et al.*, 2020; Sanità *et al.*, 2022b). The Wm composition depends on the relative proportions of the end-members celadonite (Cel), muscovite (Ms) and pyrophyllite (Prl), which are mostly controlled by the Tschermak and Pyrophyllite substitutions (see Guidotti and Sassi, 1998 for a review).

By combining the *T* and *P* ranges obtained from the Chl-Qz-H<sub>2</sub>O and Phg-Qz-H<sub>2</sub>O methods respectively, the *P-T* estimates were calculated using Chl-Phg-Qz-H<sub>2</sub>O multi-equilibrium thermobarometry (Vidal and Parra, 2000, see supplementary material S4 for more details). Only the Chl-Wm couples whose *P-T* equilibrium was within the *P* and *T* ranges calculated with the two other methods were considered. For this selected group of *P-T*

values, a further equilibrium tolerance was set to consider only the  $P$ - $T$  values to which the minimum Gibbs free energy ( $<5000$  J in this case) is related. Finally, to verify the robustness of our results, a comparison between the classic geo-thermobarometers available in the literature was performed (i.e. Massonne and Schreyer, 1987; Bourdelle and Cathelineau, 2013; Lanari *et al.*, 2014c). According to Vidal and Parra (2000), the absolute uncertainty on  $T$  and  $P$  estimates are of  $\pm 30^\circ\text{C}$  and  $\pm 0.2$  GPa, respectively.

#### White mica 'crystallinity' index and $b_0$ cell parameters

X-ray diffraction was used to obtain the WmIC and  $b_0$  cell parameters (see supplementary material S5 for more details about the sample preparation). The WmIC was measured on the  $<2$   $\mu\text{m}$  grain-size glycolated powder fraction that was placed on glass slides following the procedure described by Lezzerini *et al.* (1995). The WmIC measures the changes in the shape (Full Width at Half Maximum, FWHM) of the first basal reflection of Wm grains by X-ray diffraction, which is considered sensitive to temperature variation (Weaver, 1961; Kübler, 1967a, 1967b; Sassi and Scolari, 1974; Kisch, 1980a, 1980b). The FWHM values expressed in  $\Delta^\circ 2\theta$  CuK $\alpha$  units of the Wm 10  $\text{\AA}$  peaks have been reported in the crystallinity index scale (CIS, Warr and Ferreiro Mählmann, 2015). The spectra of each investigated sample are reported in fig. F3 in the supplementary material S5.

The  $b_0$  parameter was calculated (Sassi and Scolari, 1974; Franceschelli *et al.*, 1989; Guidotti and Sassi, 1989) by measuring the  $d_{060}$  spacing in white mica grains using the (211) quartz reflection as an internal standard (i.e. Kisch *et al.*, 2006). The positions of Wm and quartz reflections were defined on randomly orientated whole-rock powders for each metapelite sample. To verify the reliability of the measurement of  $b_0$  in this work, we performed a further calculation of this parameter using the compositions of Wm, which were observed to be in textural equilibrium with Chl using the equations proposed by Guidotti and Sassi (1989) included in the spreadsheet of Verdecchia *et al.* (2019). The authors take into account different cation occupancies of Wm, where the condition  $\text{Na}/(\text{Na}+\text{K}) < 0.15$  is obeyed to calculate the parameters:  $b_0 = 8.9931 + 0.0440(\text{Mg}^{2+} + \text{Fe}^{2+} + \text{Fe}^{3+})$ ;  $b_0 = 9.1490 - 0.0258(\text{Al}^{\text{IV}} + \text{Al}^{\text{VI}})$ ; and  $b_0 = 8.5966 + 0.0666(\text{Si})$ . Finally, to verify the robustness of our results for WmIC and  $b_0$ , a comparison with data published in the literature by different authors in the same tectonic unit was performed.

## Results

### Mineral compositions

#### Chlorite

All the compositional heterogeneity of Chl grains grown along the S1 foliation (D1 chlorites) were considered. Note, that the quality of the compositions of Chl described in this section were evaluated following the recommendations proposed by Vidal and Parra (2000). Although the chlorite investigated is located in the same microdomain (white box of Fig. 3e), compositional differences exist (Fig. 4a,b). At the microscale (Figs 3e,4a), detrital Chl along the S0 appears as large stocky crystals with frayed edges and has a MgO-rich composition (up to 15 wt.%) compared to the neo-formed S1 Chl (which tends to have ca 10 wt.% of MgO, yellow line in Fig 4a). The latter is characterized by crystals with well defined edges never exceeding 20–30  $\mu\text{m}$  in size (Fig. 3e). Overall, a core-to-rim decrease of the MgO content can be observed. FeO wt.%

tends to be higher in the core of both detrital and syn-metamorphic Chl (Fig. 4b). The  $\text{Al}_2\text{O}_3$  wt.% map of Fig. 4c shows an enlarged area of the Chl grains that grew along the S1 foliation (white boxes of Fig. 4a and b). At least three groups of Chl can be detected (blue, red and green areas in Fig. 4c), whose average compositions with the related standard deviations are reported in Table 1. The first group is characterised by  $\text{Al}_2\text{O}_3$  of ca. 23.00 wt.%; the second group tends to have slightly higher  $\text{Al}_2\text{O}_3$  content (with a mean of 23.27 wt.%) whereas the third group has a more scattered  $\text{Al}_2\text{O}_3$  content with a mean of 21.87 wt.%. *XMapTools* allows fine-scale selection of pixels located in different areas of the X-ray compositional maps. This tool allowed us to investigate small areas (a few  $\mu\text{m}$ -size) of Chl crystals in which the compositions cannot be acquired by EPMA. For each Chl group, the structural formulae were calculated on 14 anhydrous oxygens. The first Chl group is characterised by an XMg mean of  $0.42 \pm 0.08$  (blue dot in Fig. 4d), Si contents of  $2.75 \pm 0.06$  atoms per formula unit (apfu, blue dot in Fig. 4d,e), and  $\text{Al}^{\text{VI}}$  content of  $1.63 \pm 0.06$  apfu (Fig. 4d). The second group of Chl is characterised by higher XMg with a mean of  $0.45 \pm 0.05$ , Si of  $2.72 \pm 0.04$  apfu, and  $\text{Al}^{\text{VI}}$  similar to the first group chlorites (Fig. 4d,e) with  $1.60 \pm 0.04$  apfu. The third group of D1 chlorites is characterised by XMg of  $0.34 \pm 0.05$ , mean Si content of  $2.77 \pm 0.07$  apfu and more variable  $\text{Al}^{\text{VI}}$  content ( $1.52 \pm 0.16$  apfu) (Fig. 4d,e). All D1 chlorite groups have Si contents that never exceed 3.00 apfu; the total contents of  $\text{Mg}^{2+}$  and  $\text{Fe}^{2+}$  present in the M octahedral site (M-site) are greater than 3.50 apfu and have vacancies of lower than 0.20 apfu (Fig. 4f). Overall, the D1 chlorite groups have clinocllore (Clc) + daphnite (Dph)-rich compositions (Fig. 4f, see also Table 1). The sudoite (Sud) content tends to progressively decrease from the first to the third group of D1 chlorites, whereas the amesite (Am) content tends to be higher in the second group of chlorites and, generally, never exceeds 30% (Fig. 4f and Table 1).

#### White mica

All chemical heterogeneities of the D1 Wm were considered, and the quality of these is based on the recommendations proposed by Vidal and Parra (2000). In common with Chl, detrital Wm also occurs as large crystals (up to 100  $\mu\text{m}$  in size) characterised by frayed edges, whereas the neo-formed Wm never exceed 20–25  $\mu\text{m}$  (Figs 3e,5). The  $\text{SiO}_2$  content ranges between 45 and 55 wt.% (Fig. 5a) and the  $\text{Al}_2\text{O}_3$  tends to be higher (up to 40 wt.%) in the detrital Wm compared to the neo-formed Wm (20–35 wt.%, Fig. 5b). However, the  $\text{Al}_2\text{O}_3$  wt.% variation at a grain-scale (Fig. 5b) reveals that differences exist for both detrital and syn-metamorphic Wm crystals with a general decreasing core-to-rim trend. Figure 5c shows an enlarged area of the X-ray compositional map (white box of Fig. 5a, b) where the variation of Si apfu for all the Wm grains along the S1 foliation is represented. The same *XMapTools* function used for the Chl grains was applied again. At least three groups of Wm have grown along the S1 foliation, and have textural equilibrium with those detected for Chl (purple box in Fig. 5c indicates the location of the Chl crystal outlined in Fig. 4c). The representative compositions for each group of Wm and the structural formulae calculated on 11 anhydrous oxygens are reported in Table 2. The first group has Si contents with an average of  $3.31 \pm 0.02$  apfu (Fig. 5c,d), and variable  $\text{Al}^{\text{VI}}$  content (average:  $1.56 \pm 0.1$  apfu, Fig. 5f,g). The XMg and K content are more variable (average:  $0.46 \pm 0.10$  and  $0.79 \pm 0.30$  apfu, respectively – Fig. 5d,e). The second group generally has lower Si contents (average:  $3.14 \pm 0.08$  apfu) and

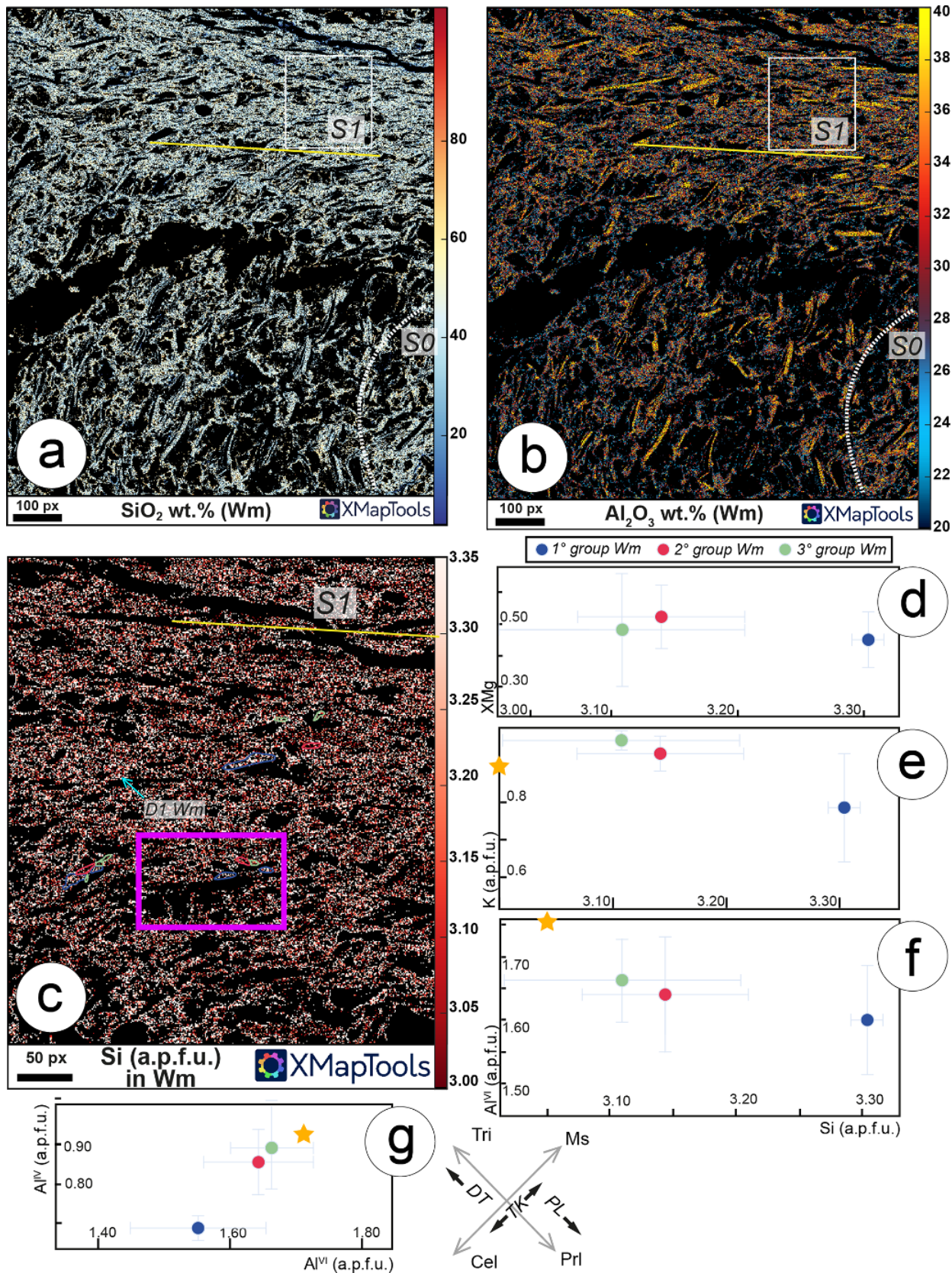


**Figure 5.** Compositions of Wm in sample ED208a. (a) SiO<sub>2</sub> wt.% and (b) Al<sub>2</sub>O<sub>3</sub> wt.% variation in the microdomain of Fig. 3e. Differences exist between detrital (white dotted line) and syn-metamorphic (yellow line) Wm grains. (c) Enlarged area of the white box of (a) and (b) of the syn-metamorphic Wm (light blue arrow) grew along the S1 foliation (yellow line). The Si content variation outlines a complex mineral chemistry of the syn-metamorphic Wm (blue, red and green areas) corresponding to first, second and third groups (see the text). The purple box indicates the Chl the location of chlorite crystal shown in Fig. 4c. (d) XMg/Si, (e) K/Si, and (f) Al<sup>IV</sup>/Si plots refer to the average composition of the three groups of Wm detected along the S1 foliation and include the related error bars. The orange stars indicate the theoretical compositional of muscovite. (g) Al<sup>IV</sup>/Al<sup>VI</sup> plot (according to Bousquet *et al.*, 2002). The grey arrows indicate the solid solution trend of Wm, while the black arrows indicate the main substitution (TK: Tschermak; DT: Di-trioctahedral; PL: Pyrophyllitic).

higher  $\text{Al}^{\text{VI}}$  contents ( $1.64 \pm 0.09$  apfu Fig. 5d–g). XMg is variable with an average of  $0.52 \pm 0.22$ , whereas the K contents tend to be less scattered (mean  $0.93 \pm 0.03$  apfu). The third group has the lowest Si content (average:  $3.11 \pm 0.1$  apfu) and the highest K content (average:  $0.98 \pm 0.01$  apfu, Fig. 5d,f). The  $\text{Al}^{\text{VI}}$  content has an average of  $1.66 \pm 0.07$  apfu, while XMg is scattered with an average of  $0.48 \pm 0.18$  (Fig. 5d,g). All Wm groups analysed can be represented by a Ms–Cel solid solution and tend to have Ms-rich compositions, with Cel and Prl contents generally not exceeding 30%, while a few Wm grains have trioctahedral (Tri) and Prl components that never exceed 25% (Table 2). According to Bousquet *et al.* (2002) the trioctahedral component could be due to the  $\text{Fe}^{3+}$  content of the Wm.

### Forward thermodynamic modelling

Phase diagrams were computed on a  $P$ – $T$  space by setting a pressure and temperature range of 0.2–1.1 GPa and 200–600°C. The KFMASH and KFMASHO systems were used, however Ca, Mn, Ti and Na were removed from the input bulk composition (see the table T4 in the supplementary material S3) because of their minor contents in the observed mineral assemblage found to be in textural equilibrium within the micro-domain of interest (white box of Fig. 3e). The model was computed considering  $\text{FeO}_{\text{tot}} = \text{Fe}^{2+}$  (Fig. 6a), as (Fe-rich) oxides in the investigated domains are scarce or absent. However, a model where  $\text{FeO}_{\text{tot}} = \text{Fe}^{2+} + \text{Fe}^{3+}$  is performed (a 10% of  $\text{FeO}_{\text{tot}}$  as  $\text{Fe}^{3+}$  as suggested by Forshaw and Pattison, 2021, see table T4 in S3) to check if the predicted mineral compositions is still comparable with the observed values (Fig. 6b). The lack of carpholite, chloritoid and biotite in the observed mineral assemblage constrains the  $P/T$  field (marked in red in Fig. 6a and b) corresponding to a  $P$  range of 1.1–0.2 GPa and a  $T$  range of 200–550°C (Fig. 6a), and to 1.0–0.2 GPa and 200–375°C in which the predicted mineral assemblage Chl, Wm and Qz matches the observed one. When  $\text{Fe}^{3+}$  is considered in the input bulk composition (Fig. 6b), the field where the observed mineral assemblage is predicted to be stable is smaller and hematite (Hem) is modelled (ca. 1%, see table T4 in S3). As the phase proportion of Fe-oxides in the investigated domains is lacking, and additionally, the modal proportion predicted by the model is low (ca. 1%), their occurrence in the  $P$ – $T$  fields of interest can be ignored. This test suggests that the observed mineral assemblage, phase proportion and compositions, can be predicted keeping  $\text{FeO}_{\text{tot}} = \text{Fe}^{2+}$  or  $\text{FeO}_{\text{tot}} = \text{Fe}^{2+} + \text{Fe}^{3+}$  (with a 10% of  $\text{FeO}_{\text{tot}}$  as  $\text{Fe}^{3+}$ ). Moreover, the amount of  $\text{Fe}^{3+}$  used in this work, given the absence of detailed information regarding mineral oxides, could be considered as the maximum value to be used for the observed mineral assemblage to be predicted (according to the suggestions proposed by Forshaw and Pattison, 2021). Ms-rich and Clc+Daph-rich compositions for Wm and Chl are predicted by both models. As the  $P$ – $T$  field for this mineral assemblage is large (Fig. 6a and b) we also computed the isopleths contoured for Si content and XMg content of Wm and Chl, respectively (Fig. 6c,d).

All computed isopleths (for Wm and Chl) intersect within the stability field of the mineral assemblage investigated. The steep trend of the XMg contour for Chl allowed us to use it as good  $T$ -sensitive parameter. For Wm, the Si isopleth shows a  $P$ - and  $T$ -dependent trend (Fig. 6b). In the model where no  $\text{Fe}^{3+}$  is considered, the predicted Si content and XMg value (for Wm and Chl, respectively) range from 3.26 and 3.36 and 0.28–0.44, respectively. Similarly, when  $\text{Fe}^{3+}$  is considered in the input bulk composition, Si content and XMg values (for Wm and Ch, respectively) are

3.26–3.34 and 0.41–0.44. Note that only the observed Si contents and XMg values of Wm ( $3.31 \pm 0.02$  apfu) and Chl ( $0.42 \pm 0.08$ ) of the first groups (see the previous section) are coherently predicted by the models. By contrast, the Si and XMg measured for the second and the third groups of Wm and Chl are not predicted by the models. Therefore, taking in mind the observed average values of Si content (for first group Wm) and XMg (for first group Chl) which can be regarded as the maximum values, it is possible to make a comparison with the modelled isopleths. In this approach, we consider that the intersection between the modelled isopleths is reliable for estimates of  $P$  and  $T$ . When  $\text{FeO}_{\text{tot}} = \text{Fe}^{2+}$  is considered, it is not possible to discriminate an area in the  $P$ – $T$  space due to a lack of clear cross-cutting relationships for the modelled isopleths corresponding to the observed average values of XMg and Si (Fig. 6c). By contrast, in the model where  $\text{Fe}^{3+}$  is considered, there is a good cross-cutting relationship between the Si and XMg isopleths for Wm and Chl, respectively, which reflects those observed and provides  $P$  and  $T$  estimates of 275–280°C and 0.85–0.80 GPa (Fig. 6d).

### Inverse modelling for $P$ – $T$ estimates

The results obtained with the Chl–Qz– $\text{H}_2\text{O}$  (Vidal *et al.*, 2005) and Phg–Qz– $\text{H}_2\text{O}$  methods allowed us to estimate the  $P$ – $T$  conditions using the local composition of each Chl and Wm group that were found to be in textural equilibrium along the S1 foliation (see the previous section). The Chl–Qz– $\text{H}_2\text{O}$  method that was applied on the three groups of Chl present in the microdomain of Fig. 4c indicates three different ranges for chlorite temperature formation (Fig. 7a). The results are reported in the distribution histograms (Fig. 7a) where along the X-axis the  $T$  is reported while the height of each bar (Y-axis) represents the number of chlorites formed in a specific temperature range. For each computation related to each Chl group, at least 10% of  $\text{Fe}^{3+}$  was estimated (using the *ChlMicaEqui* minimization function) at fixed pressure values (0.7, 0.5 and 0.4 GPa for the first, second and third group of Chl, respectively, see the S4 for details). The temperature ranges (Fig. 7a) correspond to the peaks of 170–240°C, 250–285°C and 300–335°C.

The  $P$  conditions were estimated using the Phg–Qz– $\text{H}_2\text{O}$  method (Dubacq *et al.*, 2010) considering only the Wm analyses contained in the  $T$  range previously defined with Chl–Qz– $\text{H}_2\text{O}$ . The  $P$  range for the Wm grains grown along the S1 foliation is thus calculated at a fixed  $T$  (275, 250 and 320°C, respectively the average  $T$  values estimated for different Chl groups) and  $\text{Fe}^{3+}$  (10–20% of  $\text{FeO}_{\text{tot}}$ ). The results are represented by a line along which the interlayer water content (in the A-site) varies by increasing or decreasing  $P$  and  $T$ . Three main  $P$  ranges can be observed, i.e. 0.38–0.21 GPa, 0.61–0.42 GPa and 0.87–0.62 GPa (Fig. 7b), supporting the proposition that different Wm groups occur along the S1 foliation according with the described mineral compositions.

The  $P$ – $T$  estimates obtained with the Chl–Phg–Qz– $\text{H}_2\text{O}$  multi-equilibrium approach (Vidal and Parra, 2000) were compared with the  $P$  and  $T$  ranges constrained with the Chl–Qz– $\text{H}_2\text{O}$  and Phg–Qz– $\text{H}_2\text{O}$  methods (Fig. 7c). The comparison sheds light on the good fit between the three different methods that mark the occurrence of three different clusters of Chl–Wm couples along the S1 foliation (Fig. 7c): (1) the first cluster is related to the peak pressure conditions (*HP*–*LT*, 0.85–0.68 GPa and 250–285°C – Fig. 7c,d); (2) the second is related to the peak temperature conditions (low pressure–high temperature – *LP*–*HT*, 0.6–0.4 GPa and 300–335°C – Fig. 7c,d); whereas (3) the third cluster is related to the Chl–Wm

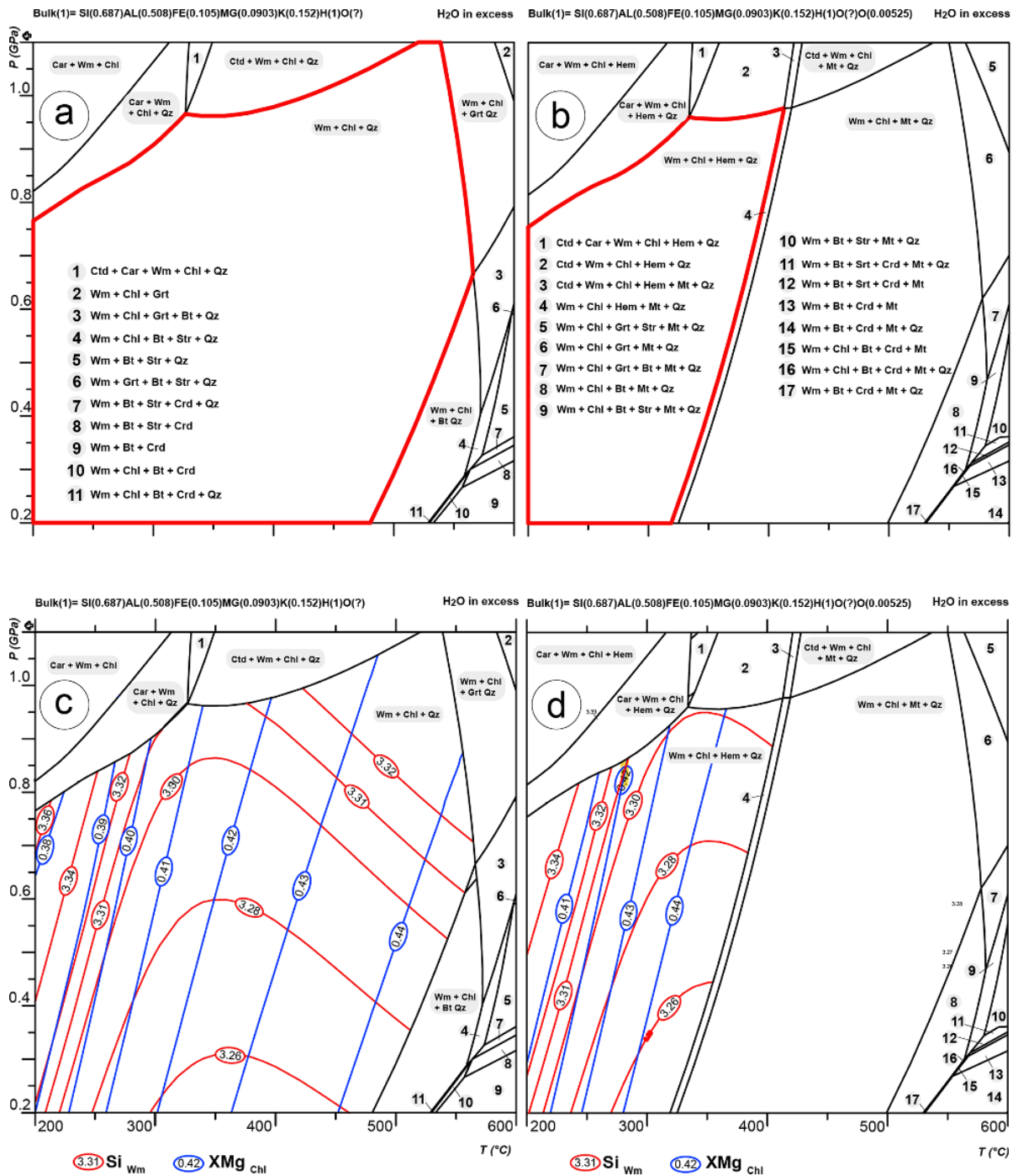


**Figure 6.** Isochemical phase diagrams related to the micro-domain within the white box of Fig. 3e. (a) Phase diagram with  $\text{FeO}_{\text{tot}}=\text{Fe}^{2+}$ . (b) Phase diagram where 10% of  $\text{FeO}_{\text{tot}}=\text{Fe}^{3+}$ . Black lines mark the boundary between different stability field, whereas the red ones indicate the field where the observed mineral assemblage is found to be stable. (c, d) Isochemical phase diagrams contoured for Si (Wm) and XMg (Chl) isopleths. The LBC is reported in moles of elements at the top of the diagrams. In the grey boxes, the stable mineral assemblages relate to the different fields are indicated. The yellow area indicates the  $P/T$  space of (d) in which the measured value of Si and XMg (for Wm and Chl, respectively) match with that predicted by the model. At the bottom of each diagram, the contour legend is reported and the numbers inside the ellipses represents values of the related observed isopleth. Car: Carpholite; Ctd: Chloritoid; Grt: Garnet; Bt: Biotite; St: Staurolite; Crd: Cordierite; Hem: Hematite; Mt: Magnetite.

couple, which is stable at the lowest  $P$  and  $T$  conditions (low pressure–low temperature –  $LP-LT$ , 0.35–0.2 GPa and 235–250°C – Fig. 7c,d).

The results obtained were compared with the pressures and temperatures estimated via classic geothermobarometers

(Fig. 7c–f). We used the calibrations proposed for low-temperature conditions by Lanari *et al.* (2014c), which can be used even if the amount of  $\text{Fe}^{3+}$  in chlorite is unknown, and by Bourdelle and Cathelineau (2015). The latter calibration was proposed by the authors as an efficient tool to estimate the temperature of chlorite

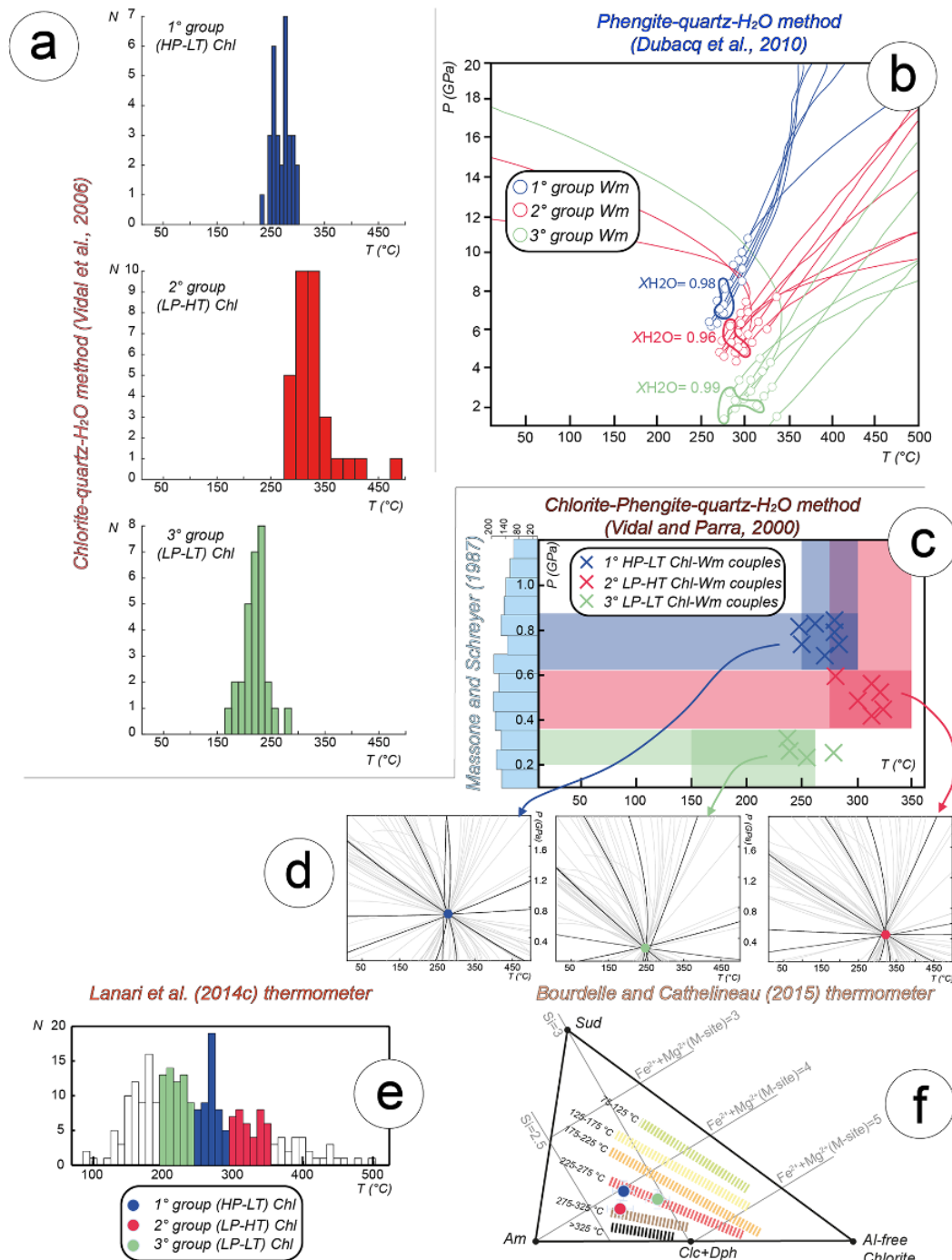


**Figure 7.** *P-T* estimate results. (a) Histograms of temperature range of Chl formation belonging to the three groups obtained with Chl-Qz-H<sub>2</sub>O. Each bar represents the counts of each chlorite whose temperature formation falls in a specific range reported along the X-axis. (b) Results of the Phg-Qz-H<sub>2</sub>O barometer. Within the *P/T* space the equilibrium lines Wm+Qz+H<sub>2</sub>O, together with only the hydration state (empty circles along each line) of white mica changes, are reported for each Wm groups. The XH<sub>2</sub>O values used in the model for each Wm group are also indicated. (c) *P/T* diagram showing the results of *P-T* estimates from the Chl-Phg-Qz-H<sub>2</sub>O method. Each cross indicates the pressure and temperature equilibrium condition for a single Chl-Wm couple belonging to the first, the second and the third groups. The blue, red and green boxes mark the temperature and pressure ranges of Chl and Wm formations obtained with the methods reported in a and b. Along the Y-axis, the histogram shows the results of the Massone and Schreyer (1987) barometer. Each bar represents the counting of pressure values for each pixel inside the micro-domain of Fig. 3e. (d) *P/T* space showing examples of all the independent (black lines) and dependent (grey lines) equilibria obtained with Chl-Phg-Qz-H<sub>2</sub>O for each Chl-Wm couple belonging to the first, the second and the third group. (e) Histograms showing the results of the Lanari et al. (2014c) geothermometer. Each bar statistically represents temperature range values of chlorite formation. (f) Diagram showing the results of the Bourdelle and Cathelineau (2015) geothermometer, where the dashed lines indicate different *T* ranges. Here, the plot of each average values referred to the different groups of chlorite are reported with their error bars.

formation (although the non-ideal contribution of site mixing is not considered) by means a graphical representation in which Fe<sup>2+</sup>

+ Mg<sup>2+</sup> (M-site) occupancy vs Si content is reported. The first geothermometer (Fig. 7e) for the different groups of chlorite grains

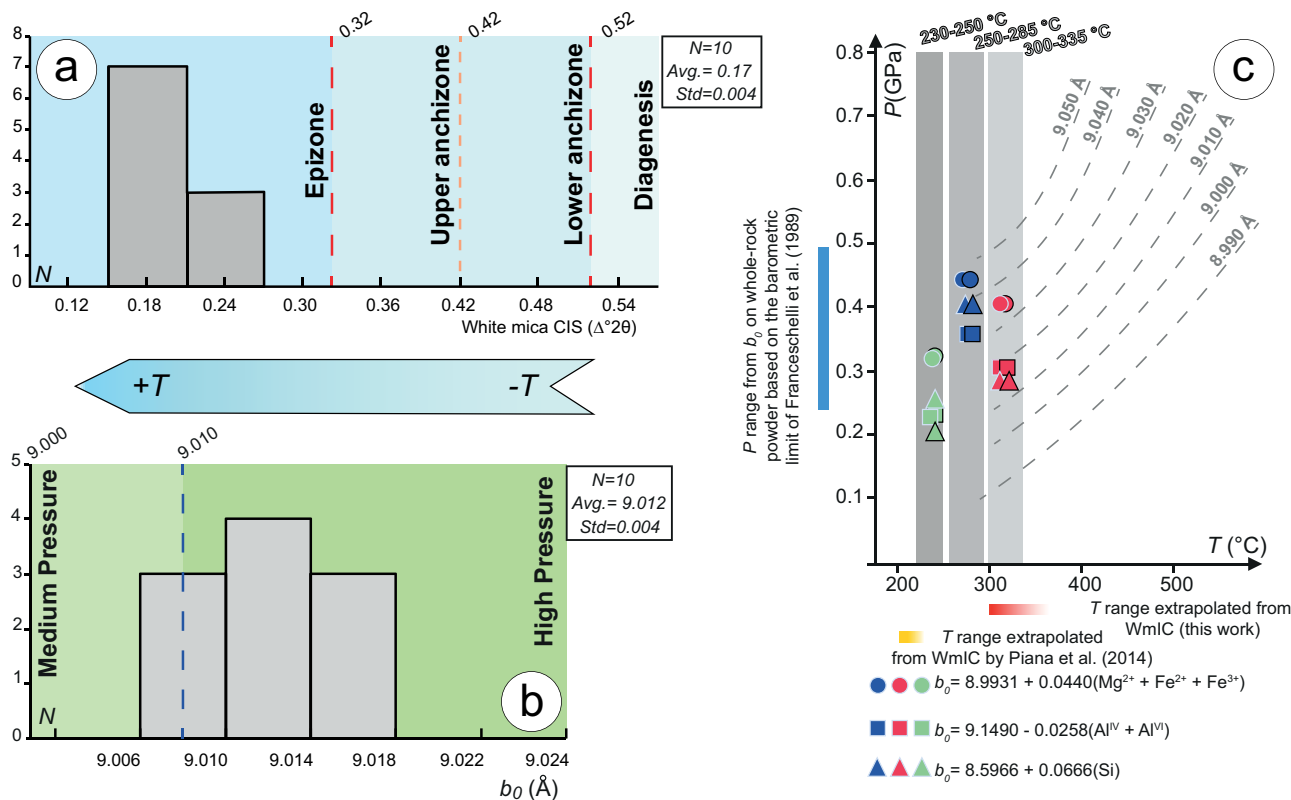


**Figure 8.** Crystallochemical indices distribution. (a) WmIC distribution. (b)  $b_0$  cell parameters distribution from XRD patterns. (c)  $b_0$  values calculated using the Verdecchia *et al.* (2019) spreadsheet. The grey rectangular boxes represent the three  $T$  ranges independently obtained with thermobaric methods. Along Y- and X-axes the crystallochemical index distribution (coloured rectangular bars) obtained using the XRD pattern analysis is reported. The  $T$  ranges calculated by Piana *et al.* (2014) are reported (yellow rectangular bar along the X-axis). The shaded effect indicates that the upper limit of the range is poorly constrained with this method. The triangles, circles and squares contoured in black are referred to the calculations in which 10% of ferric iron is considered.

indicates the following  $T$  ranges: 250–270°C for the first group (HP–LT chlorites); 310–320°C for the second group (LP–HT chlorites); and 180–240°C for the third group (LP–LT chlorites). The Bourdelle and Cathelineau (2015) geothermometer (Fig. 7f) yields three different  $T$  ranges: the first range is 225–275°C; the second is 275–325/ >325°C; and the third again 225–275°C. Altogether, these comparisons show a good fit with the three temperature ranges of chlorite formations modelled with multi-equilibrium thermobarometry. The geobarometer of Massonne and Schreyer (1987) (Fig. 7c) was used to test our  $P$  estimates. This geobarometer is based on a calibration where the (Fe, Mg) celadonite component of Wm, which is in equilibrium with K-Fsp + Qz + Phlogopite (Phl), is a function of pressure. The pressure range calculated on the Wm grains (values >200 pixel/map) grown along the S1 foliation (histogram reported along the Y-axis of Fig. 7c) is 1.2–0.2 GPa, with a peak at 0.5–0.2 GPa.

#### WmIC and $b_0$

The WmIC values with the relative standard deviation, measured along the investigated transect, are shown in the histogram of Fig. 8a. The red dashed lines indicate the lower and upper limits of very low-grade metamorphic conditions proposed by Warr and Ferreiro Mählmann (2015). Overall, specimens have fewer variable WmIC distributions, ranging from 0.13 to 0.22  $\Delta^\circ 2\theta$  (Fig. 8a and table T5 in the supplementary material S5). Mixed layers are not identified (see fig. F2 in supplementary material S5). These data

strongly indicate that the Cabanaira Unit reached typical epizone  $T$  conditions (more than 300°C) during its deformation history. Overall, the distribution of the WmIC values into the Cabanaira Unit is in good agreement with the microstructural observations and the observed paragenesis.

The  $b_0$  value distribution is represented in the histograms of Fig. 8b, with the barometric limit values (blue dashed lines) suggested by Franceschelli *et al.* (1989). Samples again show less variability in the distribution values of the  $b_0$  cell parameter, with values ranging between 9.006 and 9.018 Å and a peak at 9.011–9.013 Å (Fig. 8b). The  $b_0$  values measured on the Cabanaira Unit are within the field related to high-pressure metamorphic field (0.5–0.2 GPa based on Franceschelli *et al.*, 1989). The calculation of the  $b_0$  parameter obtained by taking into account the average compositions of white mica groups (according to Verdecchia *et al.*, 2019) found to be in equilibrium with chlorite grains along the S1 foliation was performed (Fig. 8c, see table T6 in supplementary materials S5). In the  $P/T$  space of Fig. 8c, the  $b_0$  isopleths (after Guidotti and Sassi, 1986) are indicated. Along the X-axes, the equivalent  $T$  range related to the measured WmIC values of powders < 2  $\mu\text{m}$ , is reported. Each point in the  $P/T$  space represents the  $b_0$  calculated for Wm average compositions related to each group at a  $T$  corresponding to that estimated for chlorite formation with the Chl-Qz-H<sub>2</sub>O thermometer of Vidal *et al.* (2005). Overall, the  $P$  ranges obtained from the calculated  $b_0$  values fall within the range estimated with that extrapolated from powder X-ray diffraction. However, these  $P$  ranges associated with the  $b_0$  values tend to

be related to lower pressure values rather than those calculated by the barometer of Dubacq *et al.* (2010) with the *HP-LT* Wm group showing the highest discrepancy.

## Discussion

### *P-T* path of the Cabanaira Unit reconstructed by an integrated approach

The integrated approach applied in this work allows us to reconstruct, for the first time, the *P-T* path for the low-grade Cabanaira Unit (Fig. 9) which is exposed along the southwestern sector of the Marguareis Massif. Microstructural analyses clearly indicate that mineral the assemblage Chl-Wm-Qz are in textural equilibrium, along the S1 foliation micro-site of interest, with no evidence of minerals like carpholite or chloritoid. The thermobarometric estimates show that the prograde path is not recorded by the unit and that the described mineral assemblages are related to the retrograde path only (Fig. 9). In the following the different approaches will be discussed taking into account their ability to capture the metamorphic history of the low-grade rocks of interest.

Forward thermodynamic modelling suggests that the observed mineral assemblage is predicted to be stable under a wide range of *P-T* conditions. However, using the isopleths approach and considering the effect of the ferric iron, the *P-T* estimates for the first group of Wm and Chl was constrained (275–280°C and 0.85–0.80 GPa). The occurrence of Wm-Chl groups showing slight differences in their compositions and the limited ability to physically select them in order to obtain at least three local bulk compositions make the usage of forward thermodynamic modelling restricted. Notwithstanding, the database used to perform forward thermodynamic modelling yielded realistic results. In fact, the adopted solution models for Wm include pyrophyllite and paragonite as end-members of white-mica solid solution. The stability of paragonite is not expected due to the very low Na-content of Wm, even though it cannot be correctly evaluated, because Na is not included in the input bulk composition. The possible formation of pyrophyllite predicted by modelling results from a miscibility gap with dioctahedral mica (see Parra *et al.*, 2002), which is not observed in the simulation performed in this work. For Chl, among the available solid-solution models, those adopted in this work (Vidal *et al.*, 2005 with the revised Margules parameters from Vidal *et al.*, 2006) have demonstrated more realistic pressure conditions for carpholite-producing reactions (see solution models of Hunziker *et al.*, 2003 where carpholite is predicted to be stable at low *P* conditions). It must be underlined that the chlorite model of Vidal *et al.* (2005), where Si > 3 apfu is not allowed and a Sud end-member is included, is not fully compatible with the Theriak-Domino algorithm in which Mg-Fe partitioning cannot be forced. However, the usage of the database of Pourteau *et al.* (2014) with the solution models chosen in this work (S3 supplementary material) during forward modelling allowed us to compute realistic phase equilibria diagrams even if the observed mineral assemblage is predicted to be stable into a field characterised by a substantial range of *P-T* conditions.

The reconstructed *P-T* path of the Cabanaira Unit reported in Fig. 9 was mostly constrained with the use of the multi-equilibrium thermobarometry. Inverse thermodynamic modelling applied to the three groups of Wm-Chl couples indicates that different peak *P* and *T* conditions were achieved along the tectono-thermal evolution of the Cabanaira Unit (Fig. 9). The peak *P* at 0.85–0.68 GPa and 250–285°C (which is coherent with the *P-T* conditions

predicted by forward modelling) were followed by decompressional warming (peak *T*) constrained by the Chl-Wm couples in chemical equilibrium at lower *P* (0.6–0.4 GPa) and higher *T* (300–335°C) conditions. Note that decompressional warming was also documented in other sectors of the Ligurian Alps (see Maino *et al.*, 2012). The last part of the *P-T* path is constrained by the Chl-Wm couples in equilibrium at the lowest *P* and *T* conditions (0.35–0.2 GPa and 235–250°C). The *P* and *T* estimates for the different groups of Chl-Wm couples show a good fit with the classic geothermobarometers that are usually used for low-grade metamorphism, with the exception of the Massonne and Schreyer (1987) barometer. The latter, in fact, gives pressure values (0.5–0.6 GPa) lower than the peak *P* estimated with multi-equilibrium thermobarometry approach. According to Guidotti and Sassi (1998), this is due to the effect of the deviation of the investigated mineral assemblage from the limiting mineral assemblage (i.e. Ms + K-Fsp + Qz + Phl) calibrated by Massonne and Schreyer (1987). In fact, these authors underline that any deviation from the assemblage used to perform their calibration can, at best, give a minimum pressure value.

The WmIC index and the  $b_0$  cell parameter calculated and measured in this work are roughly related to *P* and *T* range which partially fit with the thermobarometric estimates. The measured WmIC distribution roughly indicates temperatures 300°C < *T* < 350°C, according to Kisch (1987), Niedermayr *et al.* (1984) and Weaver and Boekstra (1984), which are coherent with the maximum *T* values (peak *T*) estimated with thermobarometry. The measured  $b_0$  value distribution indicates a *P* range related to 0.4–0.6 GPa for the Wm grains (Guidotti and Sassi, 1989; Guidotti *et al.*, 1989; Franceschelli *et al.*, 1989). The calculated  $b_0$  parameters for the Wm crystals used for thermobarometric calculations further provide constraints. The most coherent data are those related to the *LP-HT* Wm, indicating a range of 0.48–0.2 GPa, showing a good fit with the measured  $b_0$  values. Note that the *P* range estimated with the  $b_0$  value tends to be slightly lower than that obtained with the Phg-Qz-H<sub>2</sub>O barometer (Dubacq *et al.*, 2010), even if they are within the uncertainty associated with the thermobarometric methods. The  $b_0$  values calculated for the *LP-LT* Wm crystals also indicate *P* conditions comparable to those estimated with thermobarometry (range of 0.32–0.18 GPa, cf. Fig. 7c and Fig. 8c). The *P* range, extrapolated through the  $b_0$  parameter, calculated for the *HP-LT* Wm chemical analysis shows significant differences compared with those estimated with thermobaric calculation (cf. Figs 7c and 8c). This can be explained considering the remarks underlined by Guidotti and Sassi (1976) and Sassi and Scolari (1974), which suggest that the  $b_0$  value measurement (or calculation) shows only a qualitative relation with *P* and it is tested only for a range never exceeding 0.6 GPa. The results beyond this value are therefore not reliable. However, crystallochemical indices measurement (according to Guidotti and Sassi, 1998; Kubler and Goy-Eggenberger, 2001; Abad and Nieto, 2007; Warr and Ferreiro Mahalman, 2015) have two limits: (1) they do not provide a quantitative estimate of *P* and *T* conditions; and (2) they were typically measured on rock powders where the microtexture is clearly not preserved. These two factors clearly represent the weakness of this method, and mistakes can be made in constraining the metamorphic history of low-grade rocks if the results obtained with these approaches are not verified and/or supported by other methods.

The ranges of *T* estimates obtained using different approaches, overall indicating no more than 350°C, are coherent with the observed microstructures resulting from dissolution and

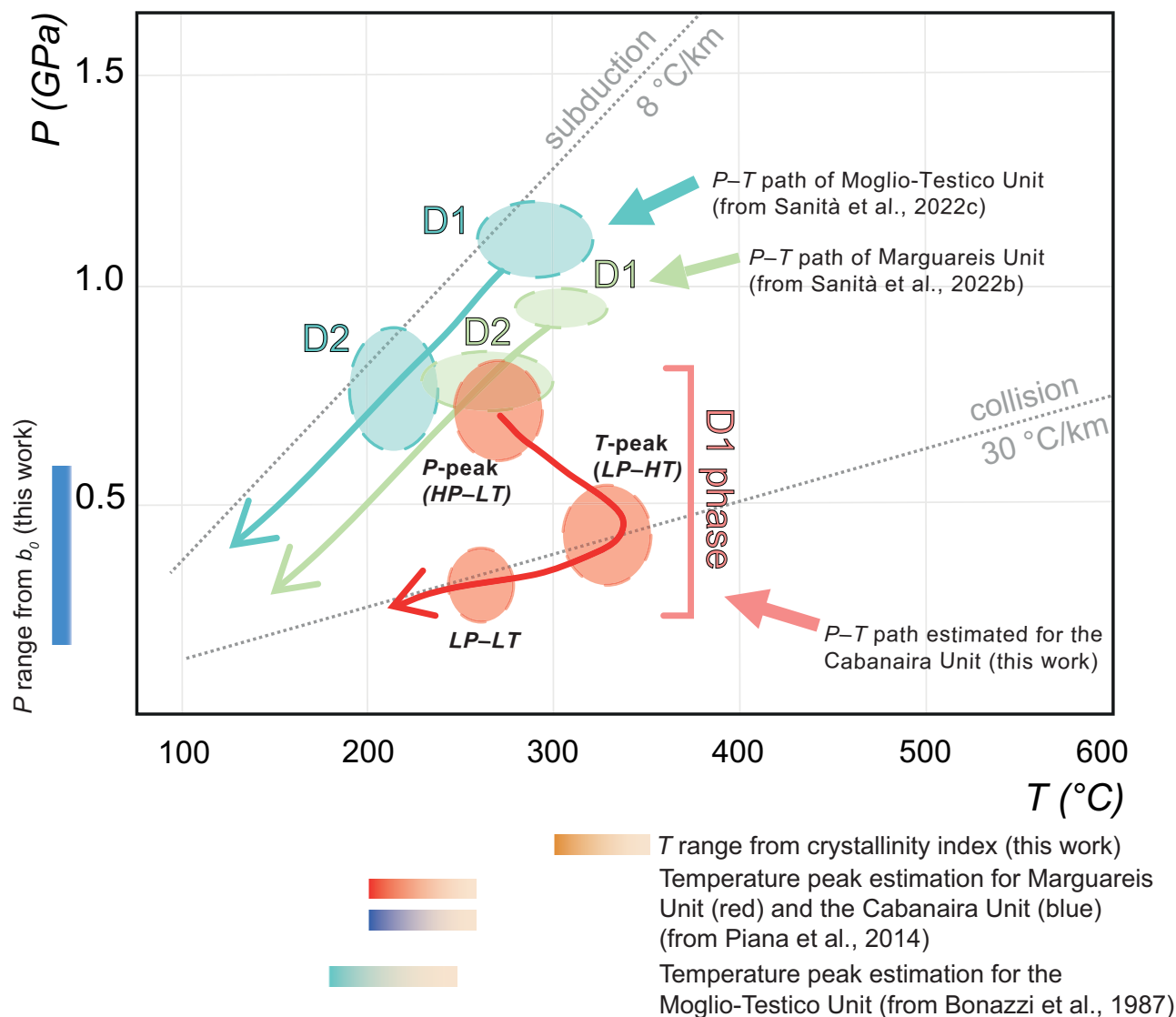


**Figure 9.** Diagram showing the  $P$ - $T$  path of the Cabanaira Unit constrained in this work. The paths estimated for the Marguareis and Moglio-Testico Unit are also represented (data from Sanità *et al.*, 2022b; 2022c). The geothermal gradients typical of subduction and collision setting are also shown. Along the X-axis the  $T$  ranges extrapolated by means Illite Crystallinity Index for the Marguareis (red rectangular bar data from Piana *et al.*, 2014), Cabanaira (blue rectangular bar from Piana *et al.*, 2014; orange rectangular bar from this work) and the Moglio-Testico (light blue rectangular bar from Bonazzi *et al.*, 1987) Units are reported. The shaded effect indicates that the upper limit of the range is poorly constrained with this method. Along the Y-axis the  $P$  range yielded from  $b_0$  measurement (this work) are reported. The length of rectangular boxes represents the range of temperature and pressure estimates.

recrystallization processes, which were the main deformation mechanisms during the metamorphic history. Similar  $T$  estimations for the deformed phyllosilicates-rich rocks have been obtained by other authors (Buatier *et al.*, 2012; Lacroix *et al.*, 2011; Lacroix and Venneman, 2015; Elmola *et al.*, 2017).

#### Assessment of the $P$ - $T$ estimates within the tectonic framework of the Cabanaira Unit

Our data indicate that the Cabanaira Unit recorded a pressure–temperature evolution where peak  $P$  conditions are followed by decompressional warming (peak  $T$ ). The consistency between this estimate and the tectonic framework proposed for the Cabanaira Unit can be assessed. The first contribution was made by Brizio *et al.* (1983), in which the authors proposed

that the thrusting of the San Remo-Monte Saccarello Unit (cf. Helminthoid Flysch Unit of this work) onto the Briançonnais Units (here represented by the Marguareis Unit, including the Cima del Becco Slices and the Cabanaira Unit) has been responsible for their deformation and the very low-grade metamorphic imprint. In this framework, the peak  $P$  conditions estimated in this work for the Cabanaira Unit should be due to the effect of the lithostatic loading produced by the thrusting of the San Remo-Monte Saccarello Unit (cf. Helminthoid Flysch Unit, this work). However, the estimated thickness of the Helminthoid Flysch Unit succession exposed in the investigated area is not sufficient to produce lithostatic loading to explain the pressure values estimated in this work for the Cabanaira Unit.

Alternatively, Piana *et al.* (2014) and d'Atri *et al.* (2016) proposed that this unit has an Anchizone metamorphic imprint, with

temperatures never exceeding 240°C during its tectonic evolution, and that it developed at very shallow structural levels. This tectonic scenario must now be reconsidered with regard to the  $P$  and  $T$  conditions constrained in this work, where temperatures greater than 300°C and pressures up to 0.8 GPa are well established.

Recently, Sanità *et al.* (2021a) and Sanità (2023) proposed a tectonic evolution in which the thrusting of the Helminthoid Flysch Unit (cf. San Remo-Monte Saccarello Unit, see *syn-stacking tectonics* of Sanità *et al.*, 2021a) developed immediately after the D1 phase recorded by the Cabanaira Unit that is thought to have developed during its involvement into the Alpine wedge (see *pre-stacking structures* of Sanità *et al.*, 2021a). The reconstructed  $P$ – $T$  pathway (Fig. 9) seems to be coherent with the tectonic setting of Sanità *et al.* (2021a, 2021b), where the tectonic evolution of the Cabanaira Unit is thought to have developed during its underthrusting, accretion and subsequent exhumation into the Alpine wedge during the middle to late Eocene. The  $P$ – $T$  paths of Fig. 9 are related to each tectonic unit exposed at the boundary between the Maritime and Ligurian Alps. In this  $P$ / $T$  space, the trajectories followed by each tectonic unit have been reconstructed using multi-equilibrium thermobarometry (see Sanità *et al.*, 2022b and 2022c for more details) making the comparison with the estimates performed in this paper justified and reliable. Note that the metamorphic peak  $P$  conditions of all the units lie along a geothermal gradient coherent with that estimated by different authors for the Western Alps for oceanic (i.e. the Moglio-Testico Unit) and continental (i.e. Margaureis Unit and Cabanaira Unit) subduction settings (Agard *et al.*, 2001; Bousquet *et al.*, 2008; Sterzynsky *et al.*, 2011; Agard *et al.*, 2018; Herviou *et al.*, 2022). Interestingly, the peak  $P$  conditions recorded by the Cabanaira Unit overlap the  $P$ – $T$  conditions estimated for the exhumation of the Marguareis Unit (see D2 phase of Sanità *et al.*, 2022b). However, only the Cabanaira Unit shows warming during decompression with the associated peak  $T$  conditions close to the classic geothermal gradient typical of the continental collision (30°C/km) estimated by previous authors for the Alpine belt.

### Factors triggering warming during the exhumation of the Cabanaira Unit

The warming event is well constrained both by multi-equilibrium thermobarometry and crystallochemical indexes measurement and it needed to be clarified. There are more factors that could trigger warming, and, in this section, they are taken into account. Below we explore all the possible processes in which warming can be developed.

(1) Thrusting-related warming. The peak  $T$  conditions estimated in this work with different methods are evidently in contrast with those calculated by Piana *et al.* (2014) (Fig. 9). These authors, through the WmIC measurement performed on the Roja Unit (cf. Cabanaira Unit of this work) estimated Anchizone field-related temperature conditions never exceeding 200–240°C by means of the WmIC parameter. Considering that the same methodology and procedure for the WmIC measurement (see Piana *et al.*, 2014 for more details) have been used, the differences between their data and the results obtained in this work could be due to the location of the sampling. In this work, sampling was performed along a transect on which structural features, such as unit-bounding thrust systems (Fig. 2a) occur. The lower crystallinity values (= higher metamorphic temperature conditions, this work), which are supported by the thermobarometric estimates, could be related to the thrust activity generally described for the whole investigated area

(Mueller *et al.*, 2020; Sanità *et al.*, 2021a; 2021b). In contrast, the higher WmIC values (= lower metamorphic temperature conditions) estimated by Piana *et al.* (2014) were obtained on samples collected in areas where tectonic structures, such as thrusts or fault systems, are lacking. Therefore, having witnessed the impact of this method, the metamorphic temperature conditions calculated in this work could be due to the effect of the thrust activity that has been documented by several authors in different tectonic settings (Fernandez-Caliani and Galan, 1992; Ducci *et al.*, 1995; Giorgetti *et al.*, 2000; Brogi, 2006; Elmola *et al.*, 2017). In this framework, the peak  $T$  calculated in this work in the investigated transect could thus be the witness of the syn-coupling tectonic events (cf. *syn-stacking* events of Sanità *et al.*, 2021a) documented in the mapped area. In this context, the warming could thus be regarded as related to the thrusting of the Helminthoid Flysch Unit onto the already exhumed Briançonnais Units (i.e. the Cabanaira Unit). Maino *et al.* (2012), (2015) and (2020) performed an investigation about the thrust activity-related thermal budget on the units exposed above and below the Penninic Front in the Monte Fronté zone. They conclude that the  $HT$  event is recorded by the rock volumes because of frictional heating due to thrust activity during nappe emplacement processes. Notwithstanding, the temperature proposed by Maino *et al.* (2020) are not coherent with those estimated in this study being ~80–90°C lower than our  $T$ -peak estimates ( $T_{max} = 245^\circ\text{C}$  vs. 300–335°C). However, comparable  $T$  estimations (>300°C) were documented by Balansa *et al.* (2023) for the Briançonnais Units exposed in the Embrunais-Ubaye sector (Western Alps, Fig. 1) and tectonically located under the Parpaillon Unit (cf. Helminthoid Flysch Unit, this work). The authors proposed that the estimated  $T$  conditions are due to the thrusting of the Parpaillon Unit onto the underlying Briançonnais Units. According to the authors, this hypothesis implies a volume for the Helminthoid Flysch Unit higher than the one shown currently. In fact, in their palinspastic reconstruction, Balansa *et al.* (2023) proposed that the leading edge of the Parpaillon Unit was located to the west of its current position. Therefore, in the investigated area, the estimated volume of the Helminthoid Flysch Unit probably does not correspond to that during the thrusting event. Therefore, a similar tectonic framework can be taken into account to explain the warming recorded by the Cabanaira Unit in the investigated area. However, this scenario is in contrast with the field constraints available for the tectonic evolution of the area of interest. In fact, according to Sanità *et al.* (2021a), the thrusting of the Helminthoid Flysch Unit postdates the folding system affecting the Cabanaira Unit (D1 phase), during which warming has been recorded.

(2) Fluid–rock interactions. Fluid–rock interaction cannot a priori be excluded. Hydrothermal circulation was documented in analogue units exposed along the outer sectors of the southwestern Alps by previous authors (cf. Entracque Unit of Barale *et al.*, 2016; Bertok *et al.*, 2018). The authors invoke the occurrence of fault systems that were used as preferred channels for hot fluid circulation. These are interpreted as responsible for the chemical transformation of the host rock and for the variation in the mineral chemistry before the deformation starts to be recorded by the unit. Moreover, fluid circulation into the subduction zone at shallower structural levels cannot be excluded. In fact, dehydration pulses within the subduction zone were outlined as key features contributing to rapid warming during the onset of exhumation (Camacho *et al.*, 2005; John *et al.*, 2012; Dragovic *et al.*, 2015), even if their role is still far from being understood. Notwithstanding, these hypotheses are in contrast with the dataset collection presented in this work because:

(i) the  $T$  estimated (at least 350°C) for the hot fluids (Barale *et al.*, 2016; Bertok *et al.*, 2018) is higher than our temperature estimates (peak  $T$ : 300–335°C); and (ii) in the study area, field evidence of an extended early faulting event was not documented, and the peak  $T$  is constrained to the deformation of the Cabanaira Unit (i.e. during its exhumation towards the surface, D1 phase). In addition, the role of fluids to the thermal budget during faulting was investigated by Maino *et al.* (2020), however, the authors concluded that fluid-rock interaction effects on the thermal budget is neglectable.

(3) Perturbation of the geothermal gradient. The warming could be due to a progressive variation in the Alpine wedge thermal state as a result of the beginning of the continental collision, which was documented in other sectors of the belt where its effects are more pronounced (Goffé *et al.*, 2004; Bousquet *et al.*, 2008; Handy *et al.*, 2010) and in Alpine Corsica (Di Rosa *et al.*, 2019; Di Rosa *et al.*, 2020 and quoted references). Many contributions have stressed the factors influencing the thermal structure of orogenic belts, such as shear and/or radioactive heating, as well as the thermal conditions of subducting and overriding plates (Gerya *et al.*, 2008; Syracuse *et al.*, 2010; Faccenna *et al.*, 2014; Zheng *et al.*, 2016; Regorda *et al.*, 2021). Anomalously high-temperature events are thought to have developed during incipient continental collision (Gerya *et al.*, 2008), even if associated with partial melting (Burg and Gerya, 2005). Amadori *et al.* (2023) proposed a geological scenario in which the mantle upwelling is invoked to account for the hot and shallow thermal signal recorded by the sediments in the late Eocene-late Miocene epi-sutural basin (i.e. the Tertiary Piedmont Basin).

Unfortunately, the current knowledge based on data presented in this work or available from previously published work is not able to provide a clear snapshot, and therefore, the hypotheses discussed in this paper need further investigation to be supported.

## Conclusions

This work outlines the paramount importance of a multidisciplinary approach to perform geological surveys aimed at investigating orogenic mechanisms recorded by very low- to low-grade units exposed in the outer sectors of collisional belts. Quantitative and qualitative methods were tested together for reconstruction of the  $P$ - $T$  path of low-grade meta-pelites, capturing as many segments of it as possible. Each method allowed us to constrain a different part of the metamorphic history of the Cabanaira Unit. The good agreement between estimates from inverse (multi-equilibrium thermobarometry) and forward modelling (pseudo-section) and crystallochemical indexes measurement, taking into consideration the strengths and weaknesses of each method, allows us to regard them as suitable to reconstruct the  $P$ - $T$  path of low-grade rocks. Multi-equilibrium thermobarometry together with high-resolution quantitative compositional mapping remain the best method to unveil the metamorphic history of low-grade rocks in details.

The  $P$ - $T$  estimates for the Cabanaira Unit indicate peak  $P$  conditions (0.85–0.68 GPa and 250–285°C) that are coherent with the geological models that imply its involvement in the subduction zone during its underthrusting and accretion into the Alpine wedge. In addition, the peak  $T$  (0.4–0.6 GPa and 300–335°C) conditions (decompressional warming) were achieved during exhumation after the peak  $P$ . The causes triggering the warming recorded by the Cabanaira Unit are far from understood, and its tectonic meaning, based on current knowledge, can only be postulated.

**Supplementary material.** Data are available from the authors on request. The supplementary material for this article can be found at <https://doi.org/10.1180/mgm.2024.80>.

**Acknowledgements.** The authors thank Tim Johnson and Arne Willner for their very useful and stimulating comments and suggestions, which improved the final version of the manuscript. We also thank the editor for managing the paper. Andrea Risplendente is thanked for his assistance with the EPMA data collection.

**Author contributions.** Conceptualization: ES; Methodology: ES, MDR; Software: ES, MDR; Validation: ES, MDR, JML, ML, MT, MM, LP; Formal analysis: ES; Investigation: ES; Resources: ES; Data Curation: ES, MDR; Writing original draft: ES; Writing - Review & Editing: ES, MDR, JML, ML, MT, MM, LP; Visualization: ES; Supervision: JML, MM, LP; Project administration: ES, LP.

**Funding statement.** This study was funded by PRIN project 2020 (PI Michele Marroni).

**Competing interests.** The authors declare none.

## References

- Abad I. and Nieto F. (2007) Physical meaning and applications of the illite Kübler index: measuring reaction progress in low-grade metamorphism. Pp. 53–64 in: *Diagenesis and Low-Temperature Metamorphism, Theory, Methods and Regional Aspects*. Seminarios, Sociedad Espanola, Sociedad Espanola Mineralogia, Spain.
- Agard P., Vidal O. and Goffé B. (2001) Interlayer and Si content of phengite in HP–LT carpholite-bearing metapelites. *Journal of Metamorphic Geology*, **19**, 479–495.
- Agard P., Plunder A., Angiboust S., Bonnet G. and Ruh J. (2018) The subduction plate interface: Rock record and mechanical coupling (from long to short timescales). *Lithos*, **320**, 537–566.
- Airaghi L., Lanari P., de Sigoyer J. and Guillot S. (2017) Microstructural vs compositional preservation and pseudomorphic replacement of muscovite in deformed metapelites from the Longmen Shan (Sichuan, China). *Lithos*, **282**, 262–280.
- Amadori C., Maino M., Marini M., Casini L., Carrapa B., Jepsen G. and Di Giulio A. (2023) The role of mantle upwelling on the thermal history of the Tertiary-Piedmont Basin at the Alps-Apennines tectonic boundary. *Basin Research*, **35**, 1228–1257.
- Balansa J., Lahfid A., Espurt N., Hippolyte J.C., Henry P., Caritg S. and Fassetieux B. (2023) Unraveling the eroded units of mountain belts using RSCM thermometry and cross-section balancing: example of the southwest-ern French Alps. *International Journal of Earth Sciences*, **112**, 443–458.
- Barale L., Bertok C., Salih Talabani N., d'Atri A., Martire L., Piana F. and Pr at A. (2016) Very hot, very shallow hydrothermal dolomitization: An example from the Maritime Alps (north-west Italy–south-east France). *Sedimentology*, **63**, 2037–2065.
- Barbero E., Di Rosa M., Pandolfi L., Delavari M., Dolati A., Zaccarini F. and Marroni M. (2023) Deformation history and processes during accretion of seamounts in subduction zones: The example of the Durkan Complex (Makran, SE Iran). *Geoscience Frontiers*, **14**, 101522.
- Beltrando M., Compagnoni R. and Lombardo B. (2010) (Ultra-) High-pressure metamorphism and orogenesis: an Alpine perspective. *Gondwana Research*, **18**, 147–166.
- Berman R.G. (1988) Internally-consistent thermodynamic data for minerals in the system Na<sub>2</sub>O–K<sub>2</sub>O–CaO–MgO–FeO–Fe<sub>2</sub>O<sub>3</sub>–Al<sub>2</sub>O<sub>3</sub>–SiO<sub>2</sub>–TiO<sub>2</sub>–H<sub>2</sub>O–CO<sub>2</sub>. *Journal of Petrology*, **29**, 445–522.
- Bertok C., Musso A., d'Atri A., Martire L. and Piana F. (2018) Geology of the Colle di Tenda–Monte Marguareis area (Ligurian Alps, NW Italy). *Journal of Maps*, **14**, 542–551.
- Bonazzi A., Cobiainchi M. and Galbiati B. (1987) Primi dati sulla cristallinit  dell'illite nelle unit  tettoniche pi  esterne e strutturalmente pi  elevate delle Alpi Liguri. *Atti Ticinensi di Scienze della Terra*, **31**, 63–77.

- Bonini L., Dallagiovanna G. and Seno S. (2010) The role of pre-existing faults in the structural evolution of thrust systems: Insights from the Ligurian Alps (Italy). *Tectonophysics*, **480**, 73–87.
- Bonnet G., Chopin C., Locatelli M., Kylander-Clark A.R. and Hacker B.R. (2022) Protracted Subduction of the European Hyperextended Margin Revealed by Rutile U-Pb Geochronology Across the Dora-Maira Massif (Western Alps). *Tectonics*, **41**, e2021TC007170.
- Bourdelle F. and Cathelineau M. (2015) Low-temperature chlorite geothermometry: a graphical representation based on a T-R<sup>2+</sup>-Si diagram. *European Journal of Mineralogy*, **27**, 617–626.
- Bousquet R., Goffé B., Vidal O., Oberhänsli R. and Patriat M. (2002) The tectono-metamorphic history of the Valaisan domain from the Western to the Central Alps: New constraints on the evolution of the Alps. *Geological Society American Bulletin*, **114**, 207–225.
- Bousquet R., Oberhänsli R., Goffé B., Wiederkehr M., Koller F., Schmid S.M. and Martinotti G. (2008) Metamorphism of metasediments at the scale of an orogen: a key to the Tertiary geodynamic evolution of the Alps. *Geological Society of London, Special Publications*, **298**, 393–411.
- Brizio D., Deregibus C., Eusebio A., Gallo M., Gosso G. and Rattalino E. (1983) Guida all'escursione: i rapporti tra la zona brianzonese ligure e il Flysch a elmintoidi, Massiccio del Marguaréis (Limone Piemonte-Certosa di Pesio, Cuneo 14/15 settembre 1983). *Memorie della Società Geologica Italiana*, **26**, 579–595.
- Broggi A. (2006) Evolution, formation mechanism and kinematics of a contractional shallow shear zone within sedimentary rocks of the Northern Apennines (Italy). *Eclogae Geologicae Helvetiae*, **99**, 29–47.
- Buatier M.D., Lacroix B., Labaume P., Moutarlier V., Charpentier D., Sizun J.P. and Travé A. (2012) Microtextural investigation (SEM and TEM study) of phyllosilicates in a major thrust fault zone (Monte Perdido, southern Pyrenees): impact on fault reactivation. *Swiss Journal of Geoscience*, **105**, 313–324.
- Burg J.P. and Gerya T.V. (2005) The role of viscous heating in Barrovian metamorphism of collisional orogens: thermomechanical models and application to the Lepontine Dome in the Central Alps. *Journal of Metamorphic Geology*, **23**, 75–95.
- Camacho A., Lee J.K., Hensen B.J. and Braun J. (2005) Short-lived orogenic cycles and the eclogitization of cold crust by spasmodic hot fluids. *Nature*, **435**, 1191–1196.
- Capponi G. and Crispini L. (2002) Structural and metamorphic signature of alpine tectonics in the Voltri Massif (Ligurian Alps, North-Western Italy). *Eclogae Geologicae Helvetiae*, **95**, 31–42.
- Capponi G. and Crispini L., Federico L., Piazza M. and Fabbri B. (2009) Late Alpine tectonics in the Ligurian Alps: constraints from the Tertiary Piedmont Basin conglomerates. *Geological Journal*, **44**, 211–224.
- Carminat E. (2001) Incremental strain analysis using two generations of syn-tectonic coaxial fibres: an example from the Monte Marguaréis Briançonnais cover nappe (Ligurian Alps, Italy). *Journal of Structural Geology*, **23**, 1441–1456.
- Chiesa S., Cortesogno L., Forcella F., Galli M., Messiga B., Pasquar G., Pedemonte G.M., Piccardo G.B. and Rossi P.M. (1975) Assetto strutturale ed interpretazione geodinamica del Gruppo di Voltri. *Bollettino della Società Geologica Italiana*, **94**, 555–581.
- Collet A., Regnault O., Ozhigin A., Imantayeva A. and Garnier L. (2022) Three-dimensional reactive transport simulation of Uranium in situ recovery: Large-scale well field applications in Shu Saryssu Basin, Tortkuduk deposit (Kazakhstan). *Hydrometallurgy*, **211**, 105873.
- Connolly J.A. (2005) Computation of phase equilibria by linear programming: a tool for geodynamic modeling and its application to subduction zone decarbonation. *Earth Planetary Science Letters*, **236**, 524–541.
- d'Atri A., Piana F., Barale L., Bertok C. and Martire L. (2016) Geological setting of the southern termination of Western Alps. *International Journal of Earth Sciences*, **105**, 1831–1858.
- De Andrade V., Vidal O., Lewin E., O'Brien P. and Agard P. (2006) Quantification of electron microprobe compositional maps of rock thin sections: an optimized method and examples. *Journal of Metamorphic Geology*, **24**, 655–668.
- de Capitani C. and Petrakakis K. (2010) The computation of equilibrium assemblage diagrams with Theriak/Domino software. *American Mineralogist*, **95**, 1006–1016.
- Decarlis A., Dallagiovanna G., Lualdi A., Maino M. and Seno S. (2013) Stratigraphic evolution in the Ligurian Alps between Variscan heritages and the Alpine Tethys opening: A review. *Earth Science Review*, **125**, 43–68.
- Di Giulio A. (1988) Structural evolution of S. Remo and Moglio-Testico units (Piemontese-Ligurian Flysch, Maritime Alps): *Abstract Rendiconti della Società Geologica Italiana*, **11**, 61–64.
- Di Giulio A. (1992) The evolution of the Western Ligurian Flysch Units and the role of mud diapirism in ancient accretionary prisms (Maritime Alps, Northwestern Italy). *Geologische Rundschau*, **81**, 655–668.
- Di Rosa M., Frassi C., Meneghini F., Marroni M., Pandolfi L. and De Giorgi A. (2019) Tectono-metamorphic evolution of the European continental margin involved in the Alpine subduction: New insights from Alpine Corsica, France. *Comptes Rendue of Geoscience*, **351**, 384–394.
- Di Rosa M., Frassi C., Malasoma A., Marroni M., Meneghini F. and Pandolfi L. (2020) Syn-exhumation coupling of oceanic and continental units along the western edge of the Alpine Corsica: A review. *Ofoliti*, **45**, 71–102.
- Dragovic B., Baxter E.F. and Caddick M.J. (2015) Pulsed dehydration and garnet growth during subduction revealed by zoned garnet geochronology and thermodynamic modeling, Sifnos, Greece. *Earth Planetary Science Letters*, **413**, 111–122.
- Dubacq B. (2008) *Thermodynamique des phyllosilicates de basse température: de l'approche macroscopique à la simulation atomistique*. Dissertation: Université Joseph-Fourier-Grenoble I, France.
- Dubacq B., Vidal O. and De Andrade V. (2010) Dehydration of dioctahedral aluminous phyllosilicates: thermodynamic modelling and implications for thermobarometric estimates. *Contribution to Mineralogy and Petrology*, **159**, 159–174.
- Ducci M., Leoni L., Marroni M. and Tamponi M. (1995) Determinazione del grado metamorfico delle Argille a Palombini dell'Alta Val Lavagna (Unità Gottero, Appennino Settentrionale). *Atti della Società Toscana di Scienze Naturali, Memorie, Serie A*, **102**, 39–45.
- Duesterhoeft E. and Lanari P. (2020) Iterative thermodynamic modelling—Part I: A theoretical scoring technique and a computer program (Bingo-Antidote). *Journal of Metamorphic Geology*, **38**, 527–551.
- Elmola A., Charpentier D., Buatier M., Lanari P. and Monie P. (2017) Textural-chemical changes and deformation conditions registered by phyllosilicates in a fault zone (Pic de Port Vieux thrust, Pyrenees). *Applied Clay Science*, **144**, 88–103.
- Faccenna C., Becker T.W., Auer L., Billi A., Boschi L., Brun J.P. and Serpelloni E. (2014) Mantle dynamics in the Mediterranean. *Review Geophysics*, **52**, 283–332.
- Fernández-Caliani J.C. and Galán E. (1992) Influence of tectonic factors on illite crystallinity: a case study in the Iberian pyrite belt. *Clay Minerals*, **27**, 385–388.
- Ford M., Duchêne S., Gasquet D. and Vanderhaeghe O. (2006) Two-phase orogenic convergence in the external and internal SW Alps. *Journal of Geological Society*, **163**, 815–826.
- Forshaw J.B. and Pattison D.R. (2021) Ferrous/ferric (Fe<sup>2+</sup>/Fe<sup>3+</sup>) partitioning among silicates in metapelites. *Contribution to Mineralogy and Petrology*, **176**, 63.
- Franceschelli M., Leoni L., Memmi I. and Puxeddu M. (1989) b0 of muscovite in low and high variance assemblages from low grade Verrucano rocks, Northern Apennines, Italy. *Schweizerische Mineralogische und Petrographische Mitteilungen*, **69**, 107–115.
- Frassi C., Di Rosa M., Farina F., Pandolfi L. and Marroni M. (2022) Anatomy of a deformed upper crust fragment from western Alpine Corsica (France): insights into continental subduction processes. *International Geology Review*, **2022**, 1–21.
- Gerya T.V., Perchuk L.L. and Burg J.P. (2008) Transient hot channels: perpetrating and regurgitating ultrahigh-pressure, high-temperature crust–mantle associations in collision belts. *Lithos*, **103**, 236–256.
- Ghignone S., Sudo M., Balestro G., Borghi A., Gattiglio M., Ferrero S. and Van Schijndel V. (2021) Timing of exhumation of meta-ophiolite units in the

- Western Alps: New tectonic implications from 40Ar/39Ar white mica ages from Piedmont Zone (Susa Valley). *Lithos*, **404**, 106443.
- Gidon M. (1972) Les chaînons Briançonnais et subBriançonnais de la rive gauche de la Stura entre le Val de l'Arma (province de Cuneo Italie). *Géologie Alpine*, **48**, 87–120.
- Giorgetti G., Memmi I. and Peacor D.R. (2000) Retarded illite crystallinity caused by stress induced sub-grain boundaries in illite. *Clay Minerals*, **35**, 693–708.
- Goffé B., Schwartz S., Lardeaux J.M. and Bousquet R. (2004) Metamorphic structure of the western and Ligurian Alps. Pp. 125–144 in: *Explanatory note to the map "metamorphic structure of the Alps"* (R. Oberhänsli, editor). Mitteilungen der Österreichischen Mineralogischen Gesellschaft, vol 149. Wien, Austria.
- Gratier J.P., Dysthe D.K. and Renard F. (2013) The role of pressure solution creep in the ductility of the Earth's upper crust. *Advances in Geophysics*, **54**, 47–179.
- Green E.C.R., White R.W., Diener J.F.A., Powell R., Holland T.J.B. and Palin R.M. (2016) Activity–composition relations for the calculation of partial melting equilibria in metabasic rocks. *Journal of Metamorphic Geology*, **34**, 845–869.
- Groppe C., Ferrando S., Gilio M., Botta S., Nosenzo F., Balestro G. and Rolfó F. (2019) What's in the sandwich? New P–T constraints for the (U) HP nappe stack of southern Dora-Maira Massif (Western Alps). *European Journal of Mineralogy*, **31**, 665–683.
- Groshong Jr R.H. (1988) Low-temperature deformation mechanisms and their interpretation. *Geological Society of American Bulletin*, **100**, 1329–1360.
- Guidotti C.V. and Sassi F.P. (1976) Muscovite as a Petrogenetic Indicator Mineral in Pelitic Schists. *Neues Jahrbuch für Mineralogie (Abhandlungen)*, **127**, 97–142.
- Guidotti C.V. and Sassi F.P. (1986) Classification and correlation of metamorphic facies series by means of Muscovite b(0) data from low-grade metapelites. *Neues Jahrbuch für Mineralogie (Abhandlungen)*, **153**, 363–380.
- Guidotti C.V. and Sassi F.P. (1998) Petrogenetic significance of Na–K white mica mineralogy: Recent advances for metamorphic rocks. *European Journal of Mineralogy*, **10**, 815–854.
- Guidotti C.V., Sassi F.P. and Blencoe J.G. (1989) Compositional controls on the a and b cell dimensions of muscovite 2Mi. *European Journal of Mineralogy*, **1**, 71–84.
- Handy M.R., Schmid S.M., Bousquet R., Kissling E. and Bernoulli D. (2010) Reconciling plate-tectonic reconstructions of Alpine Tethys with the geological–geophysical record of spreading and subduction in the Alps. *Earth Science Review*, **102**, 121–158.
- Herviou C., Agard P., Plunder A., Mendes K., Verlaquet A., Deldicque D. and Cubas N. (2022) Subducted fragments of the Liguro-Piemont ocean, Western Alps: Spatial correlations and offscraping mechanisms during subduction. *Tectonophysics*, **827**, 229267.
- Hirth G. and Tullis J.A.N. (1992) Dislocation creep regimes in quartz aggregates. *Journal of Structural Geology*, **14**, 145–159.
- Holland T.J.B. and Powell R. (2011) An improved and extended internally consistent thermodynamic dataset for phases of petrological interest, involving a new equation of state for solids. *Journal of Metamorphic Geology*, **29**, 333–383.
- Hunziker P. (2003) The stability of tri-octahedral Fe<sup>2+</sup>–Mg–Al chlorite. A combined experimental and theoretical study. Dissertation. Universität Basel, Switzerland.
- John T., Gussone N., Podladchikov Y.Y., Bebout G.E., Dohmen R., Halama R. and Seitz H.M. (2012) Volcanic arcs fed by rapid pulsed fluid flow through subducting slabs. *Nature Geosciences*, **5**, 489–492.
- Kisch H.J. (1980a) Incipient metamorphism of Cambro-Silurian clastic rocks from the Jämtland Supergroup, Central Scandinavian Caledonides, Western Sweden: illite crystallinity and vitrinite reflectance. *Journal of Geological Society*, **137**, 271–288.
- Kisch H.J. (1980b) Illite crystallinity and coal rank associated with lowest-grade metamorphism of the Tavayanne greywacke in the Helvetic zone of the Swiss Alps. *Swiss Journal of Geosciences*, **73**, 753–777.
- Kisch H.J. (1987) Correlation between indicators of very low-grade metamorphism. Pp. 227–300 in: *Low Temperature Metamorphism* (Frey M., editor). Blackie & Son, Glasgow.
- Kisch H.J., Sassi R. and Sassi F.P. (2006) The b0 lattice parameter and chemistry of phengites from HP/LT metapelites. *European Journal of Mineralogy*, **18**, 207–222.
- Kubler B. (1967a) La cristallinité de l'illite et les zones tout à fait supérieures du métamorphisme. Pp. 105–122 in: *Colloque sur le "Étages tectoniques"*. Festschrift, Institut de géologie de l'université de Neuchâtel, Switzerland.
- Kubler B. (1967b) Anchimétamorphisme et schistosité. *Bulletin Centre de Recherches de Pau SNPA*, **1**, 259–278.
- Kubler B. and Goy-Eggenberger D. (2001) The crystallinity of illite revisited: a review of knowledge acquired. *Clay Minerals*, **36**, 143–157.
- Lacroix B. and Vennemann T. (2015) Empirical calibration of the oxygen isotope fractionation between quartz and Fe–Mg-chlorite. *Geochemica and Cosmochimica Acta*, **149**, 21–31.
- Lacroix B., Buatier M., Labaume P., Trave A., Dubois M., Charpentier D., Ventalon S., Convert-Gaubier D. (2011) Microtectonic and geochemical characterization of thrusting in a foreland basin: example of the South-Pyrenean orogenic wedge (Spain). *Journal of Structural Geology*, **33**, 1359–1377.
- Lagabrielle Y., Brovarone A.V. and Ildefonse B. (2015) Fossil oceanic core complexes recognized in the blueschist metaophiolites of Western Alps and Corsica. *Earth Science Review*, **141**, 1–26.
- Lanari P. (2012) *Micro-cartographie P-T dans les roches métamorphiques. Applications aux Alpes et à l'Himalaya*. Dissertation. Université de Grenoble, France.
- Lanari P. and Duesterhoeft E. (2019) Modeling metamorphic rocks using equilibrium thermodynamics and internally consistent databases: Past achievements, problems and perspectives. *Journal of Petrology*, **60**, 19–56.
- Lanari P. and Engi M. (2017) Local bulk composition effects on metamorphic mineral assemblages. Pp. 55–102 in: *Petrochronology: Methods and Applications* (Matthew J. Kohn, Martin Engi, Pierre Lanari, editors). Reviews in Mineralogy and Geochemistry, **83**. The Geochemical Society and The Mineralogical Society of America, Chantilly, Virginia, USA.
- Lanari P., Guillot S., Schwartz S., Vidal O., Tricart P., Riel N. and Beyssac O. (2012) Diachronous evolution of the alpine continental subduction wedge: evidence from P–T estimates in the Briançonnais Zone houillère (France–Western Alps). *Journal of Geodynamics*, **56**, 39–54.
- Lanari P., Rolland Y., Schwartz S., Vidal O., Guillot S., Tricart P. and Dumont T. (2014a) P–T–t estimation of deformation in low-grade quartz-feldspar-bearing rocks using thermodynamic modelling and 40Ar/39Ar dating techniques: example of the Plan-de-Phasy shear zone unit (Briançonnais Zone, Western Alps). *Terra Nova*, **26**, 130–138.
- Lanari P., Vidal O., De Andrade V., Dubacq B., Lewin E., Grosch E.G. and Schwartz S. (2014b) XMapTools: A MATLAB®-based program for electron microprobe X-ray image processing and geothermobarometry. *Computers and Geosciences*, **62**, 227–240.
- Lanari P., Wagner T. and Vidal O. (2014c). A thermodynamic model for di-trioctahedral chlorite from experimental and natural data in the system MgO–FeO–Al<sub>2</sub>O<sub>3</sub>–SiO<sub>2</sub>–H<sub>2</sub>O: applications to P–T sections and geothermometry. *Contributions to Mineralogy and Petrology*, **167**, 1–19.
- Lanari P., Vho A., Bovay T., Airaghi L. and Centrella S. (2019) Quantitative compositional mapping of mineral phases by electron probe micro-analyser. *Geological Society of London, Special Publications*, **478**, 39–63.
- Lardeaux J.M. (2014) Deciphering orogeny: a metamorphic perspective. Examples from European Alpine and Variscan belts Part II: Variscan metamorphism in the French Massif Central–A review. *Bulletin de la Société Géologique de France*, **185**, 281–310.
- Lardeaux J.M. and Spalla M.I. (1991) From granulites to eclogites in the Sesia zone (Italian Western Alps): a record of the opening and closure of the Piedmont ocean. *Journal of Metamorphic Geology*, **9**, 35–59.
- Lezzerini M., Sartori F. and Tamponi M. (1995) Effect of amount of material used on sedimentation slides in the control of illite "crystallinity" measurements. *European Journal of Mineralogy*, **7**, 819–823.
- Lotout C., Poujol M., Pitra P., Anczkiewicz R. and Van Den Driessche J. (2020) From burial to exhumation: Emplacement and metamorphism of mafic eclogitic terranes constrained through multimethod petrochronology, case study from the Lévézou Massif (French Massif Central, Variscan Belt). *Journal of Petrology*, **61**, ega046.

- Luoni P., Zanoni D., Rebay G. and Spalla M.I. (2019) Deformation history of Ultra High-Pressure ophiolitic serpentinites in the Zermatt-Saas Zone, Créton, Upper Valtournanche (Aosta Valley, Western Alps). *Ofoliti*, **44**, 111–123.
- Maino M. and Seno S. (2016) The thrust zone of the Ligurian Penninic basal contact (Monte Fronté, Ligurian Alps, Italy). *Journal of Maps*, **12**, 341–351.
- Maino M., Dallagiovanna G., Dobson K.J., Gaggero L., Persano C., Seno S. and Stuart F.M. (2012) Testing models of orogen exhumation using zircon (U–Th)/He thermochronology: Insight from the Ligurian Alps, Northern Italy. *Tectonophysics*, **560**, 84–93.
- Maino M., Casini L., Ceriani A., Decarlis A., Di Giulio A., Seno S. and Stuart F.M. (2015) Dating shallow thrusts with zircon (U–Th)/He thermochronometry-The shear heating connection. *Geology*, **43**, 495–498.
- Maino M., Casini L., Boschi C., Di Giulio A., Setti M. and Seno S. (2020) Time-dependent heat budget of a thrust from geological records and numerical experiments. *Journal of Geophysics Research: Solid Earth*, **125**, e2019JB018940.
- Manatschal G., Chenin P., Hauptert I., Masini E., Frasca G. and Decarlis A. (2022) The importance of rift inheritance in understanding the early collisional evolution of the Western Alps. *Geosciences*, **12**, 434.
- Marmo B.A., Clarke G.L. and Powell R. (2002) Fractionation of bulk rock composition due to porphyroblast growth: effects on eclogite facies mineral equilibria, Pam Peninsula, New Caledonia. *Journal of Metamorphic Geology*, **20**, 151–165.
- Marotta A.M., Roda M., Conte K. and Spalla M.I. (2018) Thermo-mechanical numerical model of the transition from continental rifting to oceanic spreading: the case study of the Alpine Tethys. *Geological Magazine*, **155**, 250–279.
- Massone H.J. and Schreyer W. (1987) Phengite geobarometry based on the limiting assemblage with K-feldspar, phlogopite and quartz. *Contributions to Mineralogy and Petrology*, **96**, 212–224.
- Michard A., Avigad D., Goffé B. and Chopin C. (2004) The high-pressure metamorphic front of the south Western Alps (Ubaye-Maira transect, France, Italy). *Schweizerische Mineralogische und Petrographische Gesellschaft*, **84**, 215–235.
- Michard A., Schmid S.M., Lahfid A., Ballèvre M., Manzotti P., Chopin C. and Dana D. (2022) The Maira-Sampeyre and Val Grana Allochthons (south Western Alps): review and new data on the tectonometamorphic evolution of the Briançonnais distal margin. *Swiss Journal of Geoscience*, **115**, 1–43.
- Molli G., Crispini L., Malusà M.G., Mosca M.G., Piana F. and Federico L. (2010) Geology of the Western Alps-Northern Apennine junction area – A regional review. *Journal of Virtual Explorer*, **36**, 1–49.
- Mueller P., Langone A., Patacci M. and Di Giulio A. (2018) Detrital signatures of impending collision: The deep-water record of the Upper Cretaceous Bordighera Sandstone and its basal complex (Ligurian Alps, Italy). *Sedimentary Geology*, **377**, 147–161.
- Mueller P., Maino M. and Seno S. (2020) Progressive deformation patterns from an accretionary prism (Helminthoid Flysch, Ligurian Alps, Italy). *Geosciences*, **10**, 26.
- Muirhead D. K., Bond C. E., Watkins H., Butler R. W. H., Schito A., Crawford Z. and Marpino A. (2020). Raman spectroscopy: an effective thermal marker in low temperature carbonaceous fold-thrust belts. *Geological Society, London, Special Publications*, **490**, 135–151.
- Niedermayr G., Mullis J., Niedermayr E. and Schramm J. -M. (1984) Zur Anchimetamorphose permo-skythischer Sedimentgesteine im westlichen Drauzug, Kärnten — Osttirol (Österreich). *Geologische Rundschau*, **73**, 207–221.
- Parra T., Vidal O. and Agard P. (2002) A thermodynamic model for Fe–Mg dioctahedral K white micas using data from phase-equilibrium experiments and natural pelitic assemblages. *Contribution to Mineralogy and Petrology*, **143**, 706–732.
- Passchier C.W. and Trouw R.A. (2005) *Microtectonics*. Springer Science & Business Media.
- Perotti E., Bertok C., d’Atri A., Martire L., Piana F. and Catanzariti R. (2012) A tectonically-induced Eocene sedimentary mélange in the West Ligurian Alps, Italy. *Tectonophysics*, **568**, 200–214.
- Piana F., Battaglia S., Bertok C., d’Atri A., Ellero A., Leoni L. and Perotti E. (2014) Illite (KI) and chlorite (AI) “crystallinity” indices as a constraint for the evolution of the External Briançonnais Front in Western Ligurian Alps (NW Italy). *Italian Journal of Geosciences*, **133**, 445–454.
- Plunder A., Agard P., Dubacq B., Chopin C. and Bellanger M. (2012) How continuous and precise is the record of P–T paths? Insights from combined thermobarometry and thermodynamic modelling into subduction dynamics (Schistes Lustrés, W. Alps). *Journal of Metamorphic Geology*, **30**, 323–346.
- Polino R., Gosso G. and Dal Piaz G.V. (1990) Un modello attualistico sulla genesi delle Alpi. *Memorie della Società Geologica Italiana*, **45**, 71–75.
- Pourteau A., Bousquet R., Vidal O., Plunder A., Duesterhoeft E., Candan O. and Oberhänsli R. (2014) Multistage growth of Fe–Mg–carpholite and Fe–Mg–chloritoid, from field evidence to thermodynamic modelling. *Contribution to Mineralogy and Petrology*, **168**, 1–25.
- Powell R., Holland T.J.B.H. and Worley B. (1998) Calculating phase diagrams involving solid solutions via non-linear equations, with examples using THERMOCALC. *Journal of Metamorphic Geology*, **16**, 577–588.
- Powell R., Guiraud M. and White R.W. (2005) Truth and beauty in metamorphic phase-equilibria: conjugate variables and phase diagrams. *The Canadian Mineralogist*, **43**, 21–33.
- Regorda A., Spalla M. I., Roda M., Lardeaux J. M. and Marotta A. M. (2021). Metamorphic facies and deformation fabrics diagnostic of subduction: Insights from 2D numerical models. *Geochemistry, Geophysics, Geosystems*, **22**, e2021GC009899.
- Roda M., Regorda A., Spalla M.I. and Marotta A.M. (2019) What drives Alpine Tethys opening? Clues from the review of geological data and model predictions. *Geological Journal*, **54**, 2646–2664.
- Rosenbaum G., Lister G.S. and Duboz C. (2002) Reconstruction of the tectonic evolution of the western Mediterranean since the Oligocene. *Journal of Virtual Explorer*, **8**, 103809.
- Rutter E.H. (1983) Pressure solution in nature, theory, and experiment. *Journal of Geological Society*, **140**, 725–740.
- Sagri M. (1984) Litologia, stratimetria e sedimentologia delle torbiditi di piana di bacino del Flysch di San Remo (Cretaceo superiore, Liguria occidentale). *Memorie della Società Geologica Italiana*, **28**, 577–586.
- Sanità E. (2023) *The complexity of shallow levels tectonics during continental collision: evidence from the boundary between Maritime and Ligurian Alps*. Dissertation. Università di Firenze, Italy.
- Sanità E., Lardeaux M., Marroni M., Gosso G. and Pandolfi L. (2021a) Structural relationships between Helminthoid Flysch and Briançonnais Units in the Marguareis Massif: A key for deciphering the finite strain pattern in the external southwestern Alps. *Geological Journal*, **56**, 2024–2040.
- Sanità E., Lardeaux J.M., Marroni M., Gosso G. and Pandolfi L. (2021b) Deciphering large-scale superposed fold systems at shallow crustal levels in collision zones: insights from the Marguareis Massif (southwestern Alps). *Journal of Maps*, **17**, 571–580.
- Sanità E., Lardeaux J.M., Marroni M. and Pandolfi L. (2022a) Kinematics of the Helminthoid Flysch–Marguareis Unit tectonic coupling: consequences for the tectonic evolution of Western Ligurian Alps. *Comptes Rendue of Géoscience*, **354**(G1), 141–157.
- Sanità E., Di Rosa M., Lardeaux J.M., Marroni M. and Pandolfi L. (2022b) Metamorphic peak estimates of the Marguareis Unit (Briançonnais Domain): New constrains for the tectonic evolution of the south-western Alps. *Terra Nova*, **34**, 305–313.
- Sanità E., Di Rosa M., Lardeaux J.M., Marroni M. and Pandolfi L. (2022c) The Moglio-Testico Unit (Ligurian Alps, Italy) as Subducted Metamorphic Oceanic Fragment: Stratigraphic, Structural and Metamorphic Constraints. *Minerals*, **12**, 1343.
- Sanità E., Di Rosa M., Lardeaux J.M., Marroni M. and Pandolfi L. (2023) Tectonic coupling of oceanic and continental units in the Southwestern Alps (Western Liguria, Italy) revealed by structural mapping. *Journal of Maps*, **19**, 1–11.
- Sassi F.P. and Scolari A. (1974) The b<sub>0</sub> value of the potassic white micas as a barometric indicator in low-grade metamorphism of pelitic schists. *Contributions to Mineralogy and Petrology*, **45**, 143–152.
- Scheffer C., Vanderhaeghe O., Lanari P., Tarantola A., Ponthus L., Photiades A. and France L. (2016) Syn-to post-orogenic exhumation of metamorphic nappes: Structure and thermobarometry of the western Attic–Cycladic metamorphic complex (Lavrion, Greece). *Journal of Geodynamics*, **96**, 174–193.

- Schmid S.M., Kissling E., Diehl T., van Hinsbergen D.J. and Molli G. (2017) Ivrea mantle wedge, arc of the Western Alps, and kinematic evolution of the Alps–Apennines orogenic system. *Swiss Journal of Geoscience*, **110**, 581–612.
- Seno S., Dallagiiovanna G. and Vanossi M. (2003) Palaeogeography and thrust development in the Penninic domain of the Western Alpine chain: examples from the Ligurian Alps. *Bollettino della Società Geologica Italiana*, **122**, 223–232.
- Seno S., Dallagiiovanna G. and Vanossi M. (2005) A kinematic evolutionary model for the Penninic sector of the central Ligurian Alps. *International Journal of Earth Science*, **94**, 114–129.
- Simon-Labric T., Rolland Y., Dumont T., Heymes T., Authemayou C., Corsini M. and Fornari M. (2009)  $^{40}\text{Ar}/^{39}\text{Ar}$  dating of Penninic Front tectonic displacement (W Alps) during the Lower Oligocene (31–34 Ma). *Terra Nova*, **21**, 127–136.
- Spear F.S., Pattison D.R. and Cheney J.T. (2016) The metamorphism of metamorphic petrology. *Geological Society of America Special Paper*, **523**, 31–74.
- Stampfli G.M., Borel G.D., Cavazza W., Mosar J. and Ziegler P.A. (2001) Palaeotectonic and palaeogeographic evolution of the western Tethys and Peri-Tethyan domain (IGCP Project 369). *Episodes*, **24**, 222–228.
- Štípská P., Powell R., Hacker B.R., Holder R. and Kylander-Clark A.R.C. (2016) Uncoupled U/Pb and REE response in zircon during the transformation of eclogite to mafic and intermediate granulite (Blanský les, Bohemian Massif). *Journal of Metamorphic Geology*, **34**, 551–572.
- Stöckhert B. and Gerya T. (2005) Pre-collisional high-pressure metamorphism and nappe tectonics at active continental margins: a numerical simulation. *Terra Nova*, **17**, 102–110.
- Strzeczynski P., Guillot S., Leloup P.H., Arnaud N., Vidal O., Ledru P., Corrioux G. and Darmendrail X. (2011) Tectono-metamorphic evolution of Briançonnais zone (Modane-Aussois and southern Vanoise units, Lyon Turin transect, Western Alps). *Journal of Geodynamics*, **56–57**, 55–75.
- Syracuse E.M., van Keken P.E. and Abers G.A. (2010) The global range of subduction zone thermal models. *Physics of The Earth and Planetary Interiors*, **183**, 73–90.
- Tinkham D.K. and Ghent E.D. (2005) Estimating PT conditions of garnet growth with isochemical phase-diagram sections and the problem of effective bulk-composition. *The Canadian Mineralogist*, **43**, 35–50.
- Tracy R.J. (1982) Compositional zoning and inclusions in metamorphic minerals. Pp. 355–397 in: *Characterization of Metamorphism through Mineral Equilibria* (John M. Ferry, editor). Reviews in Mineralogy and Geochemistry, **10**. Mineralogical Society of America, Washington, DC.
- Tricart P., Schwartz S., Sue C., Poupeau G. and Lardeaux J.M. (2001) La dénudation tectonique de la zone ultra-dauphinoise et l'inversion du front briançonnais au sud-est du Pelvoux (Alpes occidentales); une dynamique miocène à actuelle. *Bulletin de la Société Géologique de la France*, **172**, 49–58.
- Vanossi M., Cortesogno L., Galbiati B., Messiga B., Piccardo G. and Vannucci R. (1984) Geologia delle Alpi Liguri: dati, problemi, ipotesi. *Memorie della Società Geologica Italiana*, **28**, 5–75.
- Verdecchia S.O., Collo G., Zandomeni P.S., Wunderlin C. and Fehrmann M. (2019) Crystallochemical indexes and geothermobarometric calculations as a multiproxy approach to PT condition of the low-grade metamorphism: The case of the San Luis Formation, Eastern Sierras Pampeanas of Argentina. *Lithos*, **324**, 385–401.
- Vidal O. and Parra T. (2000) Exhumation paths of high-pressure metapelites obtained from local equilibria for chlorite–phengite assemblages. *Geological Journal*, **35**, 139–161.
- Vidal O., Goffé B. and Theye T. (1992) Experimental study of the stability of sudoite and magnesiochlorite and calculation of a new petrogenetic grid for the system  $\text{FeO-MgO-Al}_2\text{O}_3\text{-SiO}_2\text{-H}_2\text{O}$ . *Journal of Metamorphic Geology*, **10**, 603–614.
- Vidal O., Goffé B., Bousquet R. and Parra T. (1999) Calibration and testing of an empirical chloritoid-chlorite Mg-Fe exchange thermometer and thermodynamic data for daphnite. *Journal of Metamorphic Geology*, **17**, 25–40.
- Vidal O., Parra T. and Trotet F. (2001) A thermodynamic model for Fe-Mg aluminous chlorite using data from phase equilibrium experiments and natural pelitic assemblages in the 100 to 600 C, 1 to 25 kb range. *American Journal of Sciences*, **301**, 557–592.
- Vidal O., Parra T. and Vieillard P. (2005) Thermodynamic properties of the Tschermak solid solution in Fe-chlorite: Application to natural examples and possible role of oxidation. *American Mineralogist*, **90**, 347–358.
- Vidal O., de Andrade V., Lewin E., Munoz M., Parra T. and Pascarelli S. (2006) P–T deformation– $\text{Fe}^{3+}/\text{Fe}^{2+}$  mapping at the thin section scale and comparison with XANES mapping: application to a garnet-bearing metapelite from the Sambagawa metamorphic belt (Japan). *Journal of Metamorphic Geology*, **24**, 669–683.
- Warr L.N. (2021) IMA–CNMNC approved mineral symbols. *Mineralogical Magazine*, **85**, 291–320.
- Warr L.N. and Mählmann R.F. (2015) Recommendations for Kübler index standardization. *Clay Minerals*, **50**, 283–286.
- Weaver C.E. (1961) Clay minerals of the Ouachita structural belt and the adjacent foreland. Pp 147–160 in: *The Ouachita Belt*. (Flaun P.T., Goldstein A.Jr., King P.B., Weaver C.E., editors) University of Texas Publication, Austin, USA.
- Weaver C.E. and Boekstra B.R. (1984) Shale-Slate Metamorphism in Southern Appalachians (USA). *Illite-Mica Development in Sedimentology*, (Weaver C.E., editor) Elsevier Science, Amsterdam, **10**, 67–97.
- White R.W., Powell R. and Johnson T.E. (2014) The effect of Mn on mineral stability in metapelites revisited: New a–x relations for manganese-bearing minerals. *Journal of Metamorphic Geology*, **32**, 809–828.
- Willner A.P. (2021) Very-low-grade metamorphism. *Encyclopedia of Geology*, **2**, 513–521.
- Xiang H. and Connolly J.A. (2022) GeoPS: An interactive visual computing tool for thermodynamic modelling of phase equilibria. *Journal of Metamorphic Geology*, **40**, 243–255.
- Zheng Y.F. and Chen Y.X. (2016) Continental versus oceanic subduction zones. *Nature Science Review*, **3**, 495–519.